PERGAMON Mathematical and Computer Modelling 37 (2003) 795–828

MATHEMATICAL AND COMPUTER MODELLING

www.elsevier.com/locate/mcm

The Validity of 2D Numerical Simulations of Vortical Structures Around a Bridge Deck

L. BRUNO*
Department of Structural Engineering
Politecnico di Torino
Viale Mattioli 39, 10126 Torino, Italy
bruno@archi.polito.it

S. KHRIS
OptiFlow, Consulting Company in Numerical Fluid Mechanics
IMT-Technopôle de Château-Gombert, Cedex 20, 13451 Marseille, France
khris@optiflow.fr

(Received February 2002; accepted April 2002)

Abstract—This paper deals with a computational study for evaluating the capability of 2D numerical simulation for predicting the vortical structure around a quasibluff bridge deck. The laminar form, a number of RANS equation models, and the LES approach are evaluated. The study was applied to the deck section of the Great Belt East Bridge. The results are compared with wind-tunnel data and previously conducted computational simulations. Sensitivity of the results with regard to the computational approaches applied for each model is discussed. Finally, the study confirms the importance of safety-barrier modelling in the analysis of bridge aerodynamics.

Keywords—Computational wind engineering, Bridge aerodynamics, Vortex shedding, Grid-based methods, Turbulence modelling.

1. INTRODUCTION

The study of aerodynamic characteristics plays a prominent role in the design of long-span bridges. In particular, the vortex-induced forces acting on the bridge deck are of great interest from the practical point of view. In fact, this phenomenon occurs at a relatively low range of wind speeds and can markedly affect the durability and serviceability of the structure.

Traditionally, these studies are experimentally carried out by means of wind-tunnel tests, which are economically burdensome and in some cases not realistic, owing to the lack of aerodynamic similitude of the model. In order to respect the conditions of aerodynamic similarity without using cumbersome models, wind-tunnel tests often employ section models in the preliminary bridge design. In fact, rigidly mounted models provide a good description of the complex flows that develop around bluff-shaped cylinders at high Reynolds numbers.

The first author wishes to express his appreciation to the Fluent Italia and the Hewlett Packard Italia Corporations.
*Author to whom all correspondence should be addressed.

0895-7177/03/$ - see front matter Typeset by AMS-TEX
PII: S0895-7177(03)00087-6

A number of fundamental studies, critically reviewed by Buresti [1], have investigated the unsteady flow around basic bluff sections, such as circular, square, or rectangular ones. The results obtained from such studies represent a useful basis for further applications in a number of industrial fields, such as bridge aerodynamics.

Generally speaking, flows of this kind are characterized by shear layers presenting marked vorticity and by massive separation which involves unsteady motion of the vortical structures around the body and in its wake. Both of these phenomena, which are strictly interconnected, play an important role in the production of aerodynamic forces in terms of mean value and frequency content. Three-dimensional structures ultimately appear in the process of wake formation despite the nominally two-dimensional geometry of the body, as a result of the vortex lines being distorted.

The case study of the rectangular section best applies to the shape of long-span bridge decks. In regard to these cylindrical bodies, it is widely recognized that their width-depth ratio B/D strongly affects the characteristics of the separated shear layer that is generated at the leading edge [2]. From this point of view, such sections are classified into two categories, namely, the "separated-type" sections (compact cross-sections) and the "reattached-type" sections (elongated cross-sections) [3]. The former are generally prone to Karman-type vortex shedding, whereas the latter present more complex phenomena, such as discontinuities in Strouhal number at $B/D = 2.8$ and $B/D = 6$ or the double mode in the lift fluctuations due to unsteady reattachment of the separated shear layer on the side surfaces at $2.0 < B/D < 2.8$ [4]. Likewise, most of the bridge decks are quite elongated ($B/D \approx 7$) so that occurrence of a reattached shear layer calls for a proper evaluation of other characteristics of the flow, such as the extent of the separation bubble, the convection of the vortices along the surfaces of the deck, and the interaction between vortices shed from the windward and leeward edges [5].

During the last decade, the advent of powerful computers has gradually introduced a complementary computational approach to the aerodynamic analysis of bridge decks. An increased efficiency (accuracy-cost ratio) is required for this approach to be attractive as against wind-tunnel tests. To achieve this goal, a number of numerical procedures have been proposed. These can be broadly classified into two main categories: simplified methods (panel methods) applied to the potential flow (see, for example, [6]), as well as approaches that involve numerical solution of the Navier-Stokes equations (NSEs). The latter category may be further classified as regards turbulence modelling into direct numerical simulation (DNS), large-eddy simulation (LES), and Reynolds-averaged Navier-Stokes (RANS) equation models.

A number of other numerical parameters have to be taken into consideration to increase the accuracy of the simulation in grid-based methods: discretization schemes in both space and time, imposed boundary conditions, extension of the computational domain in two or three dimensions, and grid size. On the other hand, 3D analysis and refinement of spatial resolution markedly inflates memory usage and processing time. For instance, Murakami [7] reports that LES computation of vortex-shedding flow past a square section requires only 60 hours for the 2D model but more than 42 days for the 3D model on a convex c240 machine. As may be readily understood, even when possible the extension of 3D simulations to industrial applications characterized by complex geometries and high Reynolds numbers (as in the case of long-span bridge decks) is likely to prove extremely burdensome and excessively time-consuming as compared to wind-tunnel tests. In order to reduce the computational costs, many authors have examined the applicability of the above-mentioned approaches to the 2D simulations of vortex-shedding flow past a square cylinder. According to the authors of the present paper, three main studies obtained the most representative results.

Tamura *et al.* [8] discussed the reliability of two-dimensional direct numerical simulation for unsteady flows around cylinder-type structures. They emphasized the importance of the mix between grid size and discretization schemes of the nonlinear convection term in order to avoid an excessive amount of numerical diffusion. According to the above authors, two-dimensional

calculations cannot properly simulate the three-dimensional structures which ultimately appear in the process of wake formation. Consequently, attention must be paid to the reliability and limitations of 2D direct numerical simulation for the above-mentioned class of flows.

More recently, Murakami *et al.* [9] predicted the vortex-shedding flow past a two-dimensional square cylinder using large-eddy simulation (LES). The standard Smagorinsky-type subgrid model was used, and the value of the Smagorinsky constant for 2D simulations was increased by 50% with respect with the Smagorinsky constant generally used in 3D simulations ($C_S = 0.10$) in order to compensate for the limited diffusion in the spanwise direction. The results of 2D and 3D LES computations were compared with those obtained using RANS models, as well as with those obtained from experiments. The results of the 3D computations present a close correspondence with the experimental results, whereas the results of the 2D LES computations present certain significant discrepancies. According to Murakami *et al.*, the energy-transfer mechanism throughout a wide spectrum range cannot be reproduced by 2D computations because it is fundamentally due to the vortex-stretching mechanism, which is essentially a 3D phenomenon.

Shimada *et al.* [3] carried out a critical review of the tests performed using RANS simulations around square sections and extended this approach to elongated rectangular sections. They demonstrated that the $k-\varepsilon$ model, which incorporates the spanwise diffusion process by an eddy viscosity, enables two-dimensional analyses even in the high Reynolds-number region. On the other hand, an incompleteness of the ensemble-averaged model was detected in the underestimated lift fluctuations for stationary reattached-type cross sections.

The study of unsteady flows around bridge decks introduces further important difficulties related both to physical and to computational aspects.

First, the Reynolds number related to such flows is very high ($1.e+5 < Re < 1.e+08$): in computational analysis, respecting this number involves particular requirements in spatial discretization.

Second, the most widely used deck sections currently adopted for long-span bridges are characterized by intermediate levels of "bluffness" (elongated sections and faces inclined windward and leeward). Consequently, the flow around them is generally characterized by small separation bubbles and shedding of vortical structures that are extremely variable in frequency and size.

Third, the actual finished bridge deck carries several items of equipment, such as side railings and crash barriers. According to various authors, the effects of such section-model details cannot be disregarded. Using flow visualization techniques in wind-tunnel tests, Bienkiewicz [10] qualitatively showed the influence of partial streamlining and traffic barriers on the vortex-induced response of bridge decks. Adopting the same approach, Scanlan *et al.* [11] pointed out the critical dependence of bridge-flutter derivatives upon even minor details, such as deck railings. They likewise identified a critical component of the experimental approach in terms of accuracy and similitude requirements in the modelling of the section details. The noticeable influence of barriers has recently been confirmed by computational simulations performed using RANS models in the case of steady flow around a streamlined deck [12].

To provide an example of such peculiarities, we shall introduce the study case adopted in the present paper. The Great Belt East Bridge (GBEB) deck is here considered as a particularly significant benchmark from the standpoint of vortex shedding for three main reasons. First, the peculiarities mentioned above fully apply to this deck. Second, large vortex-induced oscillations were measured on the main span just after the deck's completion. Third, the deck has been the subject of various experimental measurements [13] and computational studies, and thus, provides a significant data base to be used for assessing new simulations.

Figure 1 is a schematic illustration of the flow pattern around the deck at $Re = U_0 B/\nu = 1.5e+5$ (where B is the deck width) and $\alpha = 0°$ using the computed instantaneous streamlines. The instants t_1 and t_2 correspond to a local maximum value and a local minimum value of the lift force, respectively. The three main characteristics may be easily recognized:

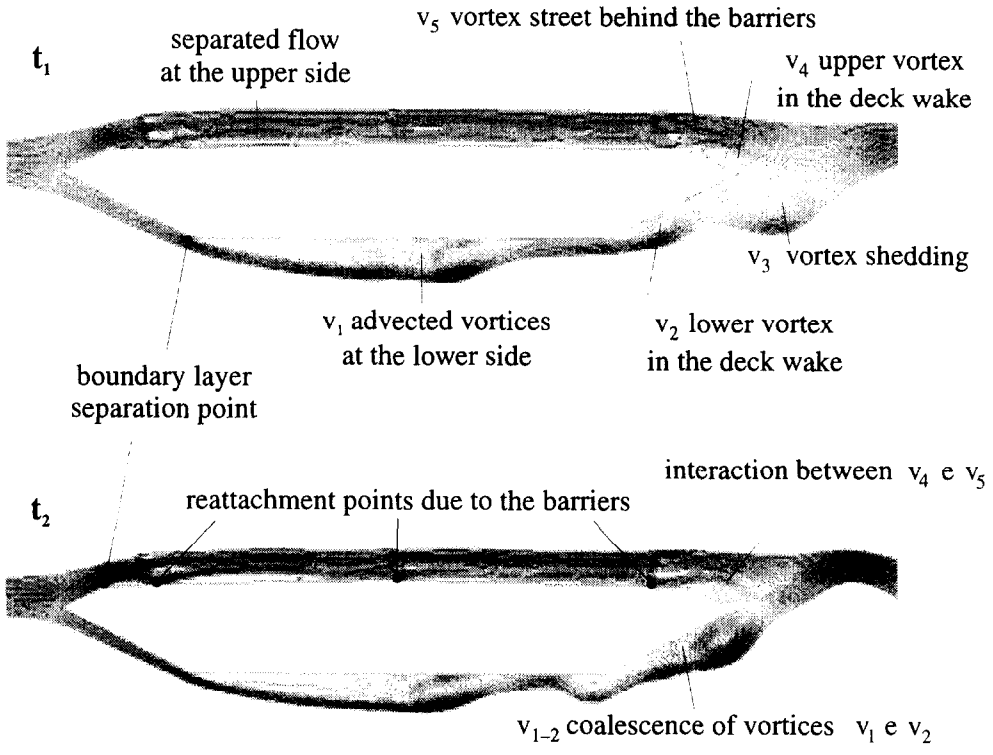

Figure 1. Flow pattern around the deck: instantaneous streamlines.

(a) the strong interaction between vortices v_1, v_2, and v_4, v_5;
(b) the differences in size, intensity, and shedding frequency between the vortices; and
(c) the flow perturbations induced by the safety barriers.

The main vortical structures around the deck are located at its lower surface and in the near wake. We shall focus on their mechanism of interaction. The vortices v_1, which develop from the separation bubble downstream of the lower sharp corner, travel across the lower surface of the deck. Independently, another recirculation zone (v_2) is present in the near-wake region close to the lower slope. When the advected procession of vortices v_1 passes the lower leeward corner, it coalesces with the vortex v_2 and is shed in the wake.

The barriers seem to enhance perturbations in the flow pattern on account of two main phenomena. First, the flow passing between the upper surface of the deck and the lateral barriers is accelerated. The side barriers reattach the separated shear layer downstream of the upwind edge and prevent a larger separation bubble from forming. Second, the vortex street v_5 behind the trailing barriers seems to interact with the vortex v_4 in the deck wake.

Table 1 summarizes the wind-tunnel setup and the conditions of computation of the most relevant studies. The results obtained are expressed in terms of the following integral parameters: the mean values of the drag coefficient $\bar{C}_D = D/(1/2\,\rho U_0 B)$ and lift coefficient $\bar{C}_L = L/(1/2\,\rho U_0 B)$, and the Strouhal number $St = f_{C_L} D/U_0$, where D is the deck depth.

Early section-model tests were conducted by Reinhold *et al.* [14] on a number of candidate cross-sectional shapes. The 1:80 model selected, designated as $H9.1$ and characterized by a width-depth ratio $B/D \approx 7.2$, was tested using equipment fully described in [14]. Steady-state wind-load coefficients were subsequently measured on the same cross section using a 1:300 taut-strip model [15]. The overall agreement between the results obtained from models of different size indicates that Reynolds-number effects, even though they are present, do not have a marked influence on the global aerodynamic behaviour of the deck. The most important discrepancy regards the value of the lift coefficient. In the opinion of the authors of the present study, this

Table 1. Outline of published studies—zero angle-of-attack ($\alpha = 0°$).

Author	Method	Model	Geom.	Re	$\bar{C}_D$	$\bar{C}_L$	St
Reinhold [14]	Exp.	Section	det	1.e + 5	0.08	+0.01	0.109 – 0.158
Larose [15]	Exp.	Taut-strip	det	7.e + 4	0.10	−0.08	0.11
Frandsen [16]	Exp.	Full scale	det	1.7e + 7	–	–	0.08 – 0.15
Larsen [17,18]	DVM	pot. + ω	2Dbas	1.e + 5	0.06	+0.06	0.100 – 0.168
Taylor [19]	DVM	pot. + ω	2Dbas	1.e + 5	0.05	+0.07	0.16 – 0.18
Frandsen [20]	DVM	pot. + ω	2Dbas	1.6e + 7	0.08	+0.06	0.09
	FEM	NSE lam	2Dbas	1.6e + 7	0.06	−0.09	0.25
Kuroda [21]	FDM	NSE lam	2Dbas	3.e + 5	0.07	−0.19	0.101 – 0.168
Selvam [22,23]	FEM	NSE les	2Dbas	1.e + 5	0.06	−0.34	0.168
Jenssen [24]	FVM	NSE les	3Ddet	4.5e + 4	0.06	+0.04	0.16
Enevoldsen [25]	FEM	NSE les	2Ddet	7.e + 4	0.07	+0.08	0.17

difference may be related to the unachieved aerodynamic similitude of the barriers in the 1:300 model. In fact, as demonstrated in [12], the most important blockage effect of the railings involves the higher flow velocity and the stronger suction along the lower surface. The lift force is thus reduced. The various vortex-shedding mechanisms highlighted in Figure 1 probably account for the spread frequency content of the lift force that was found experimentally by Reinhold *et al.* [14]. The full-scale measurements obtained by Frandsen [16] substantially confirm this characteristic of the flow. The results obtained by Larose [15] seem to indicate that the Strouhal number at the lower bound of the range has the most important effects on the structural response of the deck.

Most of the computational simulations assume the same Reynolds number used by Reinhold *et al.* [14]; exceptions are represented by [26,27]. On the other hand, only Enevoldsen *et al.* [25,28] state that they include the deck equipment in the computational model. No author takes into account the inflow turbulent level experimentally set at $I_t \approx 7.5\%$.

Three general conclusions may be drawn from an overall analysis of the results obtained. In the first place, the underestimated prediction of the drag coefficient is a common feature in all of the simulations. This error is certainly due to the absence of barriers and to the incoming smooth flow. Second, most of the simulations fail to highlight the spread frequency content of the lift force, indicating only one Strouhal number. This difficulty mainly concerns the approaches that solve the Navier-Stokes equations using grid-based methods. Finally, almost all the simulations are conducted in the 2D computational domain. This common approach provides confirmation of the fact that 3D simulations remain scarcely applicable in extended parametric studies and excessively burdensome for industrial applications.

A number of applications are based on the so-called discrete vortex method (DVM), which is comprehensively reviewed in [29]. This approach is widely adopted in bridge aerodynamics (see, for example, [6]) for two main reasons. First, the Lagrangian nature of the method markedly reduces the difficulties encountered in grid-based methods (mesh quality, numerical diffusion, modelling of small details of the deck section). Second, the description of the flow field is obtained by an essentially potential-flow method, so that the computational effort is significantly reduced as compared to the methods involving solution of the Navier-Stokes equations.

On the other hand, the above advantages are obtained thanks to a fundamental assumption regarding the physical feature of the flow, namely that "for high Reynolds numbers, viscous effects may not be essential in the development of the wake, as the vorticity that is introduced in the wake from the separation point remains confined to narrow regions and its dynamics is mainly dominated by convection, with viscous diffusion only playing a secondary role" [1]. From the numerical point of view, this assumption requires that the amount of vorticity ω shed from the separation point (which must be known *a priori*) be introduced by means of particles of finite core size in each time step. This approach has been applied to the study case by Larsen

et al. [17,18], who obtained an impressive agreement between their results and the experimental data, even if compared with more complex approaches. According to Sarpkaya [29], "practically all applications of vortex models to unsteady separated flows past two-dimensional bluff bodies have shown that the circulation of the vortices should be reduced as a function of time and space in *ad hoc* manner in order to bring the calculated forces, pressure and circulations in close agreement with those measured". As a result, the evaluation of the performance of this approach and of its suitability for application to other shapes remains very problematical. In the framework of the aforesaid numerical approach, Taylor and Vezza [19] attribute the underestimated value of the drag coefficient to the lack of modelling of the barriers. Consequently, the side railings are introduced by addition of a flat plate treated as a solid geometry. According to these authors, "care must be taken when analysing these results as [...] porosity effects are neglected"; i.e., the blockage effect is largely overestimated in such a way as to change the nature of the flow completely.

Other authors have predicted the flow around the Great Belt East Bridge by solving the Navier-Stokes equations using a number of discretization methods, e.g., finite difference method, finite element method, finite volume method.

Among the various works that neglect turbulence modelling (laminar form), the results obtained by Kuroda [21] are in good agreement with the wind-tunnel data. It seems that the error in approximating the convection term provides a numerical damping that balances the absence of turbulence damping. On the other hand, no parametric studies are reported on the relationship between numerical diffusion, grid resolution, and the scheme adopted (fifth-order upwinding) in order to justify the accuracy obtained in a 2D simulation.

More recently, Frandsen *et al.* [27] applied the FEM-without-turbulence model to the study case. A parametric study on the mesh-density sensitivity was initiated with particular attention paid to boundary-layer modelling. As a result, shedding-frequency predictions were generally inaccurate even for the most refined grid so that the authors of the paper concluded that "further studies are needed to establish the model requirements". Subsequently, Frandsen [20] tested the DVM in order to compare the two different approaches with one another and with the results of other studies.

To the knowledge of the present authors, RANS models have never been applied to the case study. Only Lee *et al.* [30] adopted a RANS approach for predicting the vortex-induced wind loading on a fully bluff bridge deck. The renormalization group (RNG) $k-\varepsilon$ model was used without law of the wall. The quadratic upwind interpolation for convective kinetics (QUICK) scheme was employed to approximate the convection term. The unsteady wind loading was indirectly validated by performing dynamic structural analysis and comparing the displacements at the bridge midspan with the full-scale measurements. This approach clearly does not permit any conclusions to be drawn on the reliability of the statistical approach.

In the last few years, the LES approach has been applied to the case study. Selvam [23] discussed the reliability of the 2D simulation, considering the deck section of the Great Belt East Bridge approach span. Both 2D and 3D computational models were used, neglecting the barriers. No parametric studies were performed. The author assumed the value of the Smagorinsky constant proposed by Murakami [9] for the square cylinder ($C_s = 0.15$ in 2D, $C_s = 0.10$ in 3D), without any further investigations. According to Selvam, only 3D models are able to capture the drag coefficient with reasonable accuracy. In a subsequent paper, the same author [22] employed two different levels of grid refinement and two near-wall treatments (i.e., low Reynolds number and law of the wall) in the 2D model of the Great Belt East Bridge main span. The results of the study indicate an impressive sensitivity of the mean flow to the parameters mentioned ($\Delta C_D \approx 50\%$, $\Delta C_L \approx 400\%$, $\Delta St \approx 20\%$). Because of the limited number of computations, no conclusions were drawn regarding this sensitivity.

In the case of nonperiodic flows and spread frequency contents of the aerodynamic forces, the integral parameters only provide a partial physical insight into the flow. Figure 2 compares the

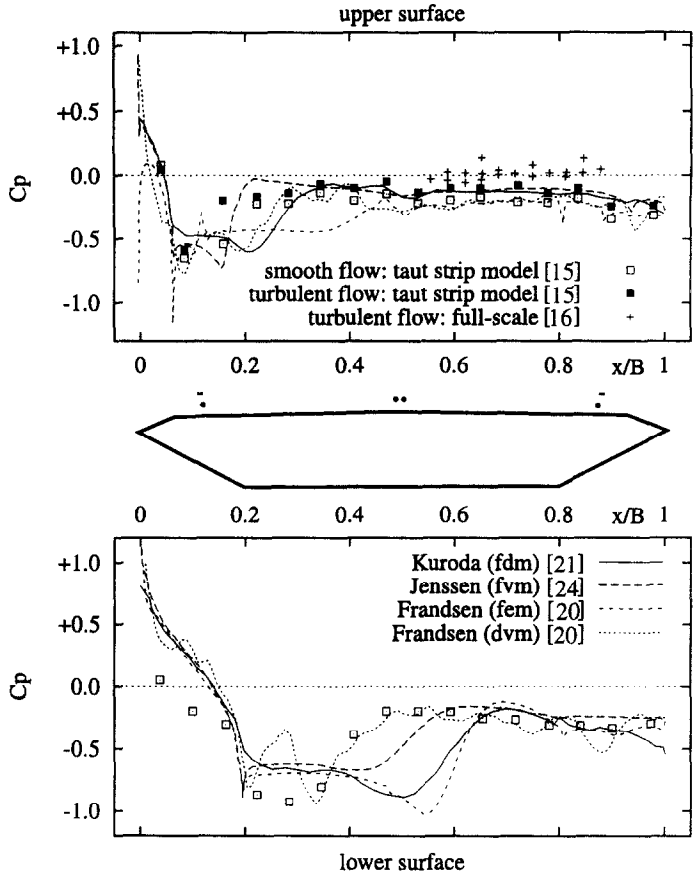

Figure 2. Published studies: mean Cp distribution on the deck ($\alpha = 0°$).

distributions of the mean pressure coefficient on the deck obtained in wind-tunnel tests and in a number of simulations. Two main discrepancies clearly appear between the experimental and the computational distributions.

First, in the range $0 \leq x/B \leq 0.2$ the experimental data reveal a moderate suction on the lower surface just downstream of the leading point. All the computational simulations ignore this phenomenon, thus overestimating the pressure. The reasons for this discrepancy are not clear. They may be related to the high anisotropy of the turbulence in the forebody region [31], but minor imperfections of the leading edge of the geometrical model cannot be ruled out *a priori*.

Second, both the lengths of the separation bubbles at the lower and upper surfaces are overestimated in the computational simulations. In the wind-tunnel tests the recirculation zone at the lower surface is restricted within the range $0.2 \leq x/B \leq 0.35$, and recovery of the pressure rapidly occurs within the range $0.35 \leq x/B \leq 0.45$. Except for the DVM approach, all the other numerical methods predict a pressure recovery in the range $0.6 \leq x/B \leq 0.7$ and underestimate the suction peak. It is to be pointed out that the phenomena occurring in this region play a major role in the vortex-formation process, as emerges from Figure 1. Consequently, the lack of accuracy in this region deeply affects the overall reliability of the simulations. The reason for these errors is not clear. However, if it is taken into account that the characteristics of the incoming flow are rather similar, the differences between computations seem to be related to the different computational procedures adopted in the studies.

The overestimated length of the bubble at the upper surface seems to be directly related to the interference effects of the windward side barrier. These effects have a minor impact on the dynamics of the flow but markedly affect the mean value of the lift force. Jenssen [24] has modelled such details, obtaining the local reattachment of the shear layer. Nevertheless, the

constant value of the pressure downstream of the railings suggests the presence of a recirculation zone that is not experimentally detected.

From the present critical review of the studies published, it follows that most of the researches primarily address the question of validation of the codes employed. In many cases, the results fail to provide any closer insight into the various physical mechanisms involved in the flow. Furthermore, the effects of various computational parameters on the solutions is not systematically clarified.

The purpose of the present paper is to reduce the incompleteness of the previous studies and to verify the suitability of 2D simulations for predicting unsteady flow past a bluff bridge deck. To do this, particular attention has been paid to determining the most suitable computational parameters to be taken into consideration in the various turbulence models. In particular, the LES approach is optimized not only as regards the above-mentioned parameters but also as regards the free input parameter of the Smagorinsky subgrid model. The suitability of each of the various approaches to turbulence is discussed on the basis of the optimized model. Finally, the equipment of the section is included in the model both to complete the experimental setup, so enabling correct comparisons to be made with wind-tunnel measurements, and to point up the effects of the details on the characteristics of the aerodynamic field.

2. GOVERNING EQUATIONS

The incompressible, unsteady, two-dimensional Navier-Stokes equations of motion are solved in the present study. The nondimensional instantaneous continuity and momentum equations are

$$\operatorname{div} \mathbf{u} = 0$$

and

$$\frac{\partial \mathbf{u}}{\partial t} + \mathbf{u} \cdot \operatorname{grad} \mathbf{u} = -\operatorname{grad} p + \frac{1}{\mathrm{Re}} \Delta \mathbf{u},$$

where $\mathbf{u}$, p, and t are, respectively, the velocity vector, pressure, and time nondimensionalized by the reference velocity U_0, the deck chord B, the air density ρ, and the kinematic viscosity ν. The Reynolds number Re results from these variables.

Both the laminar-state (i.e., without turbulence modelling) approach LAM and various turbulence-modelling approaches are applied. In the framework of the statistical approach, both first-order closure models and a second-order closure model are adopted. The first-order closure models are the standard (STD) [32] and the renormalization group (RNG) [33] forms of the $k-\varepsilon$ model. The Reynolds-averaged incompressible Navier-Stokes equations are expressed as

$$\frac{\partial U_i}{\partial t} + U_j \frac{\partial U_i}{\partial x_j} = -\frac{\partial}{\partial x_i}\left(\frac{p}{\rho} + \frac{2}{3}k\right) + \frac{\partial}{\partial x_j}\left(\nu + \nu_t\right) S_{ij}, \tag{3}$$

where ν_t is the isotropic eddy viscosity given as $\nu_t = \rho C_\mu k^2/\varepsilon$, k is the turbulent kinetic energy, and S_{ij} is the mean flow strain rate expressed as follows:

$$S_{ij} = \left(\frac{\partial U_i}{\partial x_j} + \frac{\partial U_j}{\partial x_i}\right).$$

According to the standard $k-\varepsilon$ model [32], the turbulent kinetic energy k and its dissipation rate ε are computed by means of their transportation equations

$$\frac{\partial k}{\partial t} + U_i \frac{\partial k}{\partial x_i} = \frac{\partial}{\partial x_j}\left[\left(\nu + \frac{\nu_t}{\sigma_k}\right)\frac{\partial k}{\partial x_j}\right] + P_k - \varepsilon \tag{4}$$

and

$$\frac{\partial \varepsilon}{\partial t} + U_i \frac{\partial \varepsilon}{\partial x_i} = \frac{\partial}{\partial x_j}\left[\left(\nu + \frac{\nu_t}{\sigma_\varepsilon}\right)\frac{\partial \varepsilon}{\partial x_j}\right] + C_{\varepsilon_1} P_k \frac{\varepsilon}{k} - C_{\varepsilon_2}\frac{\varepsilon^2}{k}, \tag{5}$$

where P_k is the production term of the turbulent kinetic energy, and the values of the empirical constant are the conventional ones [32].

In order to cope with the well-known excessive production of turbulent kinetic energy of this model in nonequilibrium situations, the $k-\varepsilon$ form suggested by the renormalization group [33] is also applied. This model introduces a further production term into the transport equation of the dissipation rate ε in the form

$$\pi = \frac{C_\mu \eta^3 (1 - \eta/\eta_0)}{1 + \beta \eta^3} \frac{\varepsilon^2}{k}, \tag{6}$$

where

$$\eta = \sqrt{2 S_{ij} S_{ij}} \frac{k}{\varepsilon}$$

and the constants η_0, β, σ_ε, σ_k, C_{ε_1}, C_{ε_2}, C_μ are given in [33].

In order to account better for important aspects of the flow-such as the anisotropy of the Reynolds stresses, the energy transfer between the turbulent flow and the mean flow, or the diffusive transport mechanisms—Franke and Rodi [31] applied the Reynolds stress model (RSM) to the calculation of vortex shedding past a square cylinder and obtained interesting results. Abandoning the isotropic eddy-viscosity hypothesis, the RSM closes the RANS equations by solving transport equations for the individual Reynolds stresses $R_{ij} = \overline{u_i' u_j'}$. Several terms in such equations are unknown, and modelling assumptions are required. In the present study, the turbulent diffusive transport term and the pressure-strain term, are respectively, expressed by the models proposed by Lien and Leschziner [34] and by Gibson and Launder [35].

Model equations for the large eddy simulation (LES) are expressed in the form

$$\frac{\partial \bar{u}_i}{\partial x_i} = 0 \tag{7}$$

and

$$\frac{\partial \bar{u}_i}{\partial t} + \bar{u}_j \frac{\partial \bar{u}_i}{\partial x_j} = -\frac{\partial}{\partial x_i}\left(\frac{\bar{p}}{\rho} + \frac{2}{3} k_{\mathrm{SGS}}\right) + \frac{\partial}{\partial x_j}\left(\nu + \nu_{\mathrm{SGS}}\right) \bar{S}_{ij}, \tag{8}$$

where the overline indicates the filtered value of the variable. The standard Smagorinsky-type subgrid scale model is employed [36]: k_{SGS} indicates the subgrid component of k, and ν_{SGS} the subgrid-scale eddy viscosity expressed by

$$\nu_{\mathrm{SGS}} = \rho L_{\mathrm{SGS}} \sqrt{2 \overline{S_{ij} S_{ij}}}. \tag{9}$$

The subgrid-scale mixing length L_{SGS} is related to the Smagorinsky constant $\mathrm{C_S}$ in 2D computations by

$$L_{\mathrm{SGS}} = \min\left(\kappa d,\, \mathrm{C_s} A^{1/2}\right), \tag{10}$$

where $\kappa = 0.42$, A is the cell surface, and d the distance between the cell and the nearest wall boundary.

2.1. Near-Wall Turbulence Modelling

Near-wall modelling has a significant impact upon the reliability of numerical simulations of wall-bounded flows. A number of works that use various turbulence models render these models suitable for application throughout the boundary layer by means of the wall-function approach. However, Franke *et al.* [31] have demonstrated that "the assumptions of a logarithmic velocity distribution and of local equilibrium of turbulence are violated in separated flows, especially near separation and reattachment regions" [31].

Bearing in mind the purpose of the present study, the low Reynolds number one-equation model ("two-layer model") has been adopted in the viscosity-affected region ($\mathrm{Re}_y = \rho \sqrt{k}\, y/\nu > 200$) in

conjunction with the statistical approach. This approach was successfully applied by Franke and Rodi [31] in the study case of the square cylinder and by Shimada and Ishihara [3] in predicting vortex shedding past rectangular cylinders. The turbulent viscosity ν_t and the dissipation rate ε are here calculated using the turbulent kinetic energy k from the relations

$$\nu_t = \rho C_\mu \sqrt{k}\, l_\mu, \qquad \varepsilon = \frac{k^{3/2}}{l_\varepsilon}. \tag{11}$$

The length scales l_μ and l_ε are expressed by the following relations:

$$l_\mu = c_l\, y \left[1 - \exp\left(-\frac{\mathrm{Re}_y}{A_\mu}\right)\right], \qquad l_\varepsilon = c_l\, y \left[1 - \exp\left(-\frac{\mathrm{Re}_y}{A_\varepsilon}\right)\right], \tag{12}$$

where the values of the constant in the formulas are taken from Chen and Patel [37].

When the LES model is applied, the wall shear stress τ_w is obtained from the laminar stress-strain relationship

$$\frac{\bar{u}}{u_\tau} = \frac{\rho u_\tau y}{\mu},$$

where $u_\tau = (\tau_w/\rho)^{0.5}$ is the friction velocity.

3. NUMERICAL PROCEDURES

Computations were carried out using the FLUENT v5.4 code, based on the finite volume method. In the grid-based method simulation of flow around complex geometries, mesh generation takes on fundamental importance. In this study, the computational domains are generated by coupling unstructured and structured mesh types by means of substructuring of the total grid. In particular, the mapped grid type is used in the near solid boundary in order to achieve fine resolution of the flow structure in this region.

The cell thickness y_w adjacent to the solid wall forms the subject of a parametric study for laminar simulations and complies with the mesh requirements of the two-layer approach in the computations using turbulent models. The computational domain and the boundary conditions are shown in Figure 3. The size of the domain is adopted consistently with the results of the parametric study reported in [12].

The pressure-velocity coupling is achieved by means of the pressure-implicit SIMPLE algorithm with splitting of operators [38], using a predictor-corrector approach to advance the momentum equation, whilst enforcing the continuity equation.

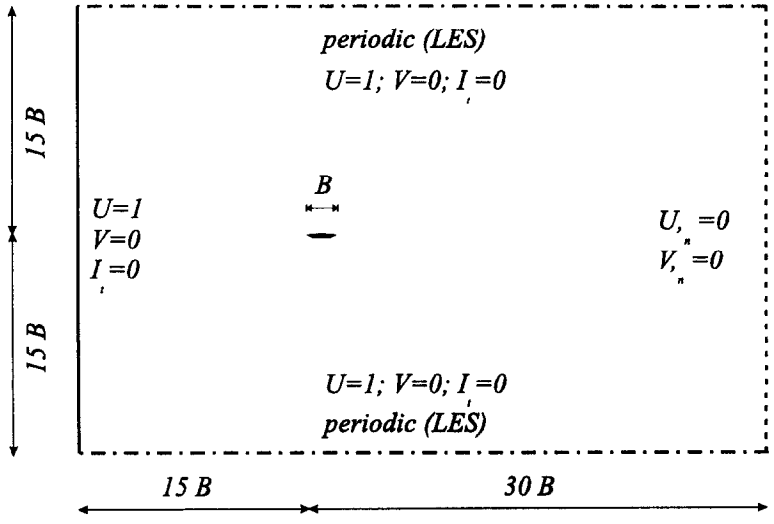

Figure 3. Analytical domain and boundary conditions.

For time discretization, the fully implicit second-order Euler scheme is adopted. The nondimensional time step in the laminar approach and statistical approach varies in the range $5.e-4 < \Delta t^* < 2.e-2$ with respect to the expected frequency content of the phenomenon and to the convergence criteria. The time advancement in LES undergoes optimization during the study. The initial conditions are set equal to the inlet boundary conditions (impulsively started simulation).

All the spatial derivative terms are discretized by the second-order central differencing, except for the nonlinear convection terms. The convection terms are discretized according to three schemes (second-order central difference, second-order upwind [39], and quadratic upwind interpolation for convective kinetics-QUICK [40]) that are generally expressed according to the formula

$$\left(U\frac{\partial f}{\partial x}\right)_i \approx \frac{1}{2}\left(u_i + |u_i|\right) d^-_{x_i} f + \frac{1}{2}\left(u_i - |u_i|\right) d^+_{x_i} f,$$

where

$$d^-_{x_i} f = \kappa_{ww} f_{ww} + \kappa_w f_w + \kappa_p f_p + \kappa_e f_e$$

and

$$d^+_{x_i} f = -\kappa_e f_e - \kappa_p f_p - \kappa_w f_w - \kappa_{ww} f_{ww}.$$

The weights for the discretization schemes adopted are given in Table 2.

Table 2. Coefficients of convective schemes.

Scheme	κ_{ww}	κ_w	κ_p	κ_e
Second-Order Central	0	$-\frac{1}{2}$	0	$\frac{1}{2}$
Second-Order Upwind	$\frac{1}{2}$	-2	$\frac{3}{2}$	0
QUICK	$\frac{1}{8}$	$-\frac{7}{8}$	$\frac{3}{8}$	$\frac{3}{8}$

As reviewed by various authors (see, for example, [41]), the odd leading-order terms (as in the case of second-order schemes) have dispersive effects—i.e., they alter the frequency content of a signal-without involving numerical diffusion. On the other hand, even leading-order terms (as in the QUICK scheme) have a diffusion effect, which generally stabilizes the computation, removing wiggles but reducing the signal in amplitude. The accuracy of the above-mentioned diffusive schemes is summarized in Table 3.

Notwithstanding the above general considerations, it is not appropriate to make universal assertions regarding the relative performance of these schemes since their performance may vary in the presence of different physical problems and according to different time-marching schemes, turbulent models (see [7,8,42]), grid density (see, for example, [8]), and computational-domain extent (i.e., 2D or 3D). The physics of the investigated flow seems to be significantly sensitive both to numerical diffusion effects (markedly affecting the small vortical structures around the deck) and to numerical dispersion effects (i.e., it appears to cause phase errors between the different shedding frequencies).

Table 3. Accuracy of convective schemes.

Scheme	Leading Term	Effect
Second-Order Central	$-\frac{(\delta_x)^2}{6}\frac{\partial^3 f}{\partial x^3} \rightarrow O\delta x^2$	dispersion
Second-Order Upwind	$-\frac{(\delta_x)^2}{8}\frac{\partial^3 f}{\partial x^3} \rightarrow O\delta x^2$	dispersion
QUICK	$-\frac{(\delta_x)^3}{12}\frac{\partial^4 f}{\partial x^4} \rightarrow O\delta x^3$	diffusion

However, even though a number of studies have been devoted to the evaluation of these schemes, in the present paper a parametric study is performed using both the laminar form and the LES approach.

4. APPLICATION AND RESULTS

4.1. Simulations Without Turbulence Modelling

The simulations assume the experimental conditions adopted by Reinhold *et al.* [14] during the section-model tests (see Table 1), except for incoming turbulence intensity $I_t = 0$. The angle of incidence of the flow is zero.

4.4.1. Effects of grid spacing and discretization schemes on the flow field

The effects of the near-wall cell thickness y_w in 2D simulations without turbulence modelling are discussed in this section. To do this, three grid systems are taken into account. These are characterized by a nondimensional grid spacing adjacent to the solid boundary equal to $y_w = 1.3\text{e}-2$, $y_w = 2.0\text{e}-3$, and $y_w = 2.2\text{e}-4$ (width $B = 1$) and will be designated in what follows respectively by lam-1, lam-2, and lam-3. The performance of these three systems is first evaluated in conjunction with a second-order upwind scheme for convection terms.

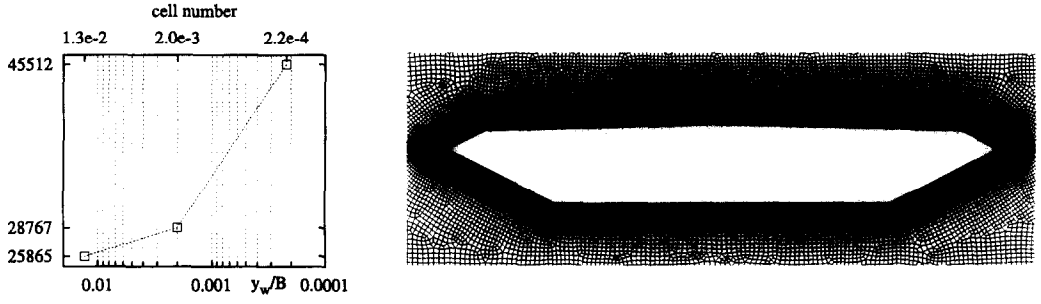

Figure 4. Near-wall cell thickness versus total number of cells (a); grid system near the deck (b).

The reduction of the first cell width involves an increased number of control volumes in the neighbourhood of the wall. The outer part of the computational domain retains the same grid. Figure 4a shows the evolution of the total number of cells of the model versus near-wall cell thickness. The close-up view of the grid system near the deck is also shown in the case of the most refined mesh (lam-3 Figure 4b).

In order to establish a relationship between the grid spacing and the simulated instantaneous flow pattern, Figure 5 shows the time history of the lift force in the range $25.6 < \Delta t < 27.6$, where the nondimensional time is expressed as $t = TU_0/B$. A number of instants are selected on the time track, and the instantaneous streamline patterns are plotted for each model. The coarsest mesh provides a steady solution, i.e., without fluctuations of the lift force. The flow remains completely attached to the deck on the side surfaces, as shown by the streamline pattern just below the diagram. The other grid systems enable observation of major fluctuations of the lift force.

The time history of the lift coefficient C_L related to the medium level of refinement appears very regular, suggesting that just one mechanism plays a dominant role in the vortex-shedding process. The flow-pattern visualizations in the left-hand side column confirm the above hypothesis. The separation bubble at the lower surface is very large, but the level of vorticity in the recirculation region seems too low to involve vortex shedding. Consequently, the vortex does not interact with the vortex developing in the near-wake region. Local maxima in the lift track ($t = 26.0$

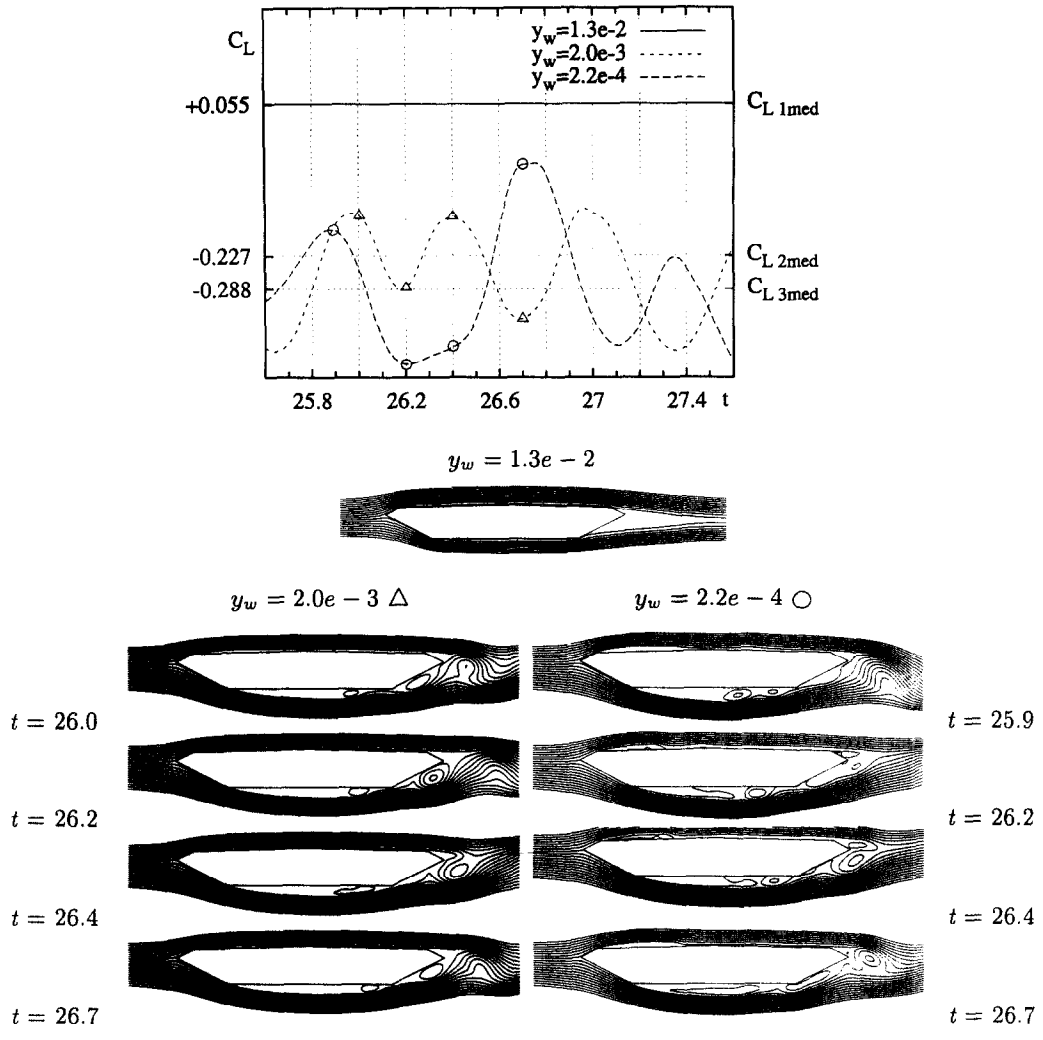

Figure 5. Time history of the lift coefficient and instantaneous streamlines.

and $t = 26.4$) are regularly observed when this vortex is shed in the wake. Conversely, the minima ($t = 26.2$ and $t = 26.7$) are related to the maximum development of the vortex close to the wall.

The grid spacing lam-3 enables detection of a fundamental feature of the flow, namely the interaction and merging between the vortices travelling along the lower surface and the vortices emerging at the downstream edges. The first maximum ($t = 25.9$) and minimum ($t = 26.2$) substantially match those simulated by means of the grid lam-2. But subsequently the lift force in the lam-2 model performs one period of oscillation between the instants $t = 26.2$ and $t = 26.7$, whereas the C_{L3} just covers a half period (local maximum at $t = 26.7$). The streamlines clearly show the merging of the vortices at that moment. The most refined grid also detects the separation bubble downstream of the windward edge at the upper surface and the clockwise circulating flow in the upper area of the deck wake. However, the role played by these structures in the vortex-shedding process does not seem to be of primary importance.

The pressure distribution on the lower surface at the above-mentioned instants is presented in Figure 6. These results confirm the differences between the models lam-2 and lam-3. In the former model the pressure fluctuations are always separated by the sharp corner at $x/B = 0.8$ without interaction. When the finest grid is used, the pressure fluctuations move backward, reducing the extent of the separation bubble. Owing to the larger amount of vorticity produced at the separation point, the pressure at $x/B = 0.8$ does not remain constant, but reaches a deep trough when the vortices at the lower surface pass the edge. It should be noted that as

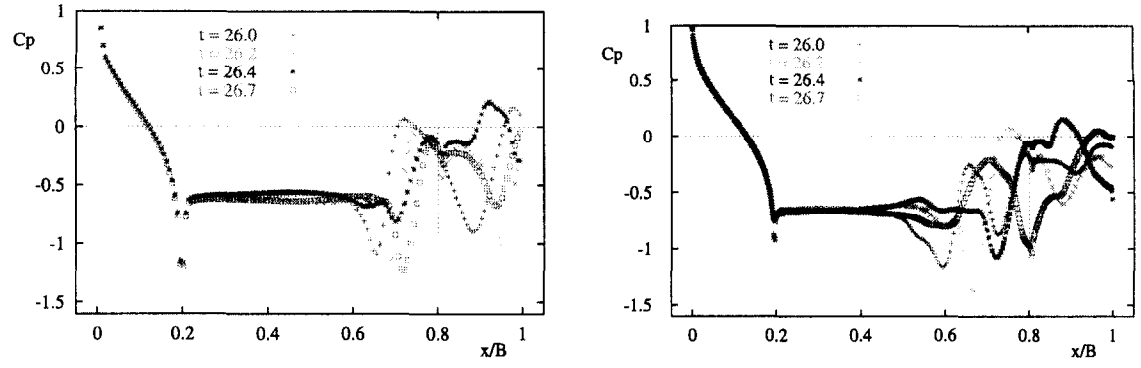

(a) $y_w = 2.0e-3$. (b) $y_w = 2.2e-4$.

Figure 6. Instantaneous distributions of the pressure coefficient Cp on the lower surface.

the grid spacing is enlarged, the model just simulates one large eddy on the side surface. This approximation does not involve major problems in the simulation of flow around bluff cylinders with sharp corners characterized by massive separation and large-sized vortices. Instead, in the case of semibluff sections, a coarse mesh completely conceals the small vortical structures at the basis of the vortex-formation process, thus leading to a fundamental error. A number of grid points is required both in order to ensure a cell size smaller than the smallest vortex length and to prevent an excessive amount of numerical diffusion related to the discretization scheme adopted for the diffusive terms.

In order to extend the discussion to the integral flow parameters in time and space, a statistical treatment of the results is called for. Figure 7a shows the C_D and C_L time traces simulated with the model lam-3. As may be readily appreciated, the signals are completely random. In a case of this sort, as has already been pointed out by Taylor [19], the extent of the sampling window is very important for the extraction of meaningful statistical parameters. To optimize the sampling extent, the computations run as long as the lower Strouhal number St_1 remains constant (see Figure 7b). Generally speaking, a sampling extent of 30 nondimensional time units is found to be required in order to assume stationarity of the signal. Since the first ten units are strongly affected by the impulsive initial condition, each simulation was conservatively extended to 50 nondimensional time units.

In what follows, the main statistical parameters of the aerodynamic behaviour of the deck are discussed.

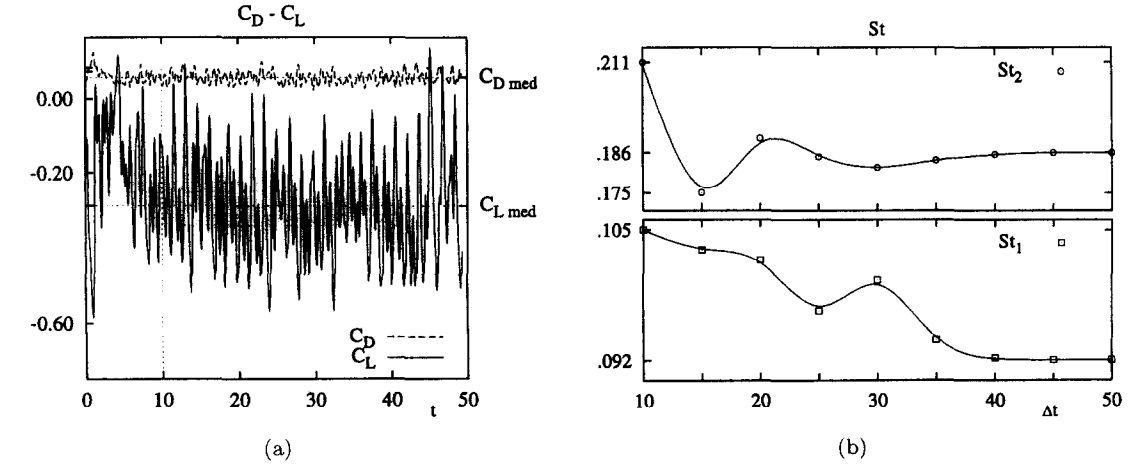

(a) (b)

Figure 7. Optimization of the extent of sampling-time.

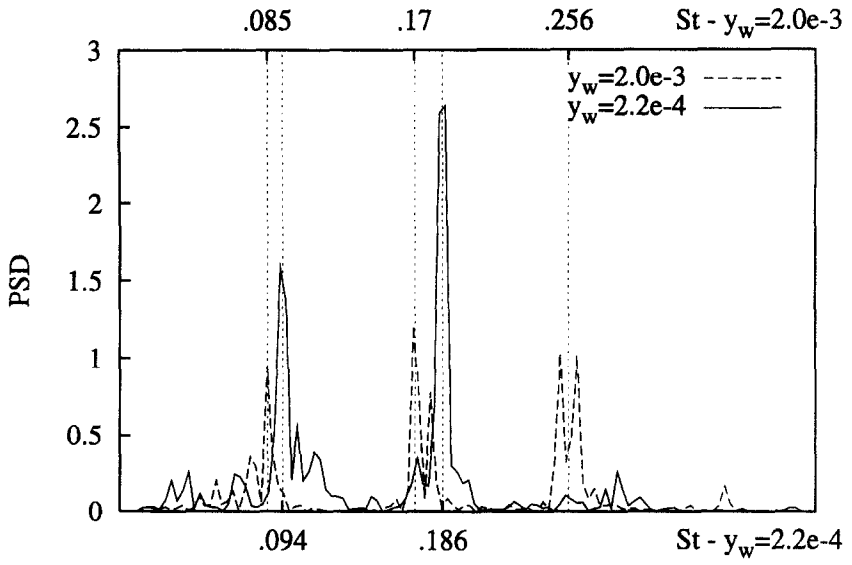

Figure 8. Effects of grid spacing on Strouhal number.

The power spectral densities (PSD) of the lift coefficient for the unsteady solutions (models lam-2 and lam-3) are plotted in Figure 8 versus the nondimensional frequency (i.e., Strouhal number). The PSD obtained from the model lam-2 is characterized by three main peaks. In effect the higher peaks correspond to frequencies that are integer multiples of the first frequency (i.e., superharmonics). This means that the physical frequency remains unique in accordance with the flow visualizations shown in Figure 5. The mean peaks in the PSD obtained from lam-3 are fewer in number. The corresponding Strouhal numbers are physically due to the different shedding mechanisms that have been described above. However, the ratio between the main Strouhal numbers ($St_2/St_1 \approx 2$) remains quite different from the experimental one ($St_2/St_1 \approx 1.67$).

The mean values of the drag and lift coefficients obtained in the computational simulations are compared with the experimental results in Figure 9. The standard deviation around the mean value is indicated by means of error bars. Even though the description of the flow field provided by Figure 5 is qualitatively complete and refers to a very likely situation, the mean values of the coefficients are not in close agreement with experiments.

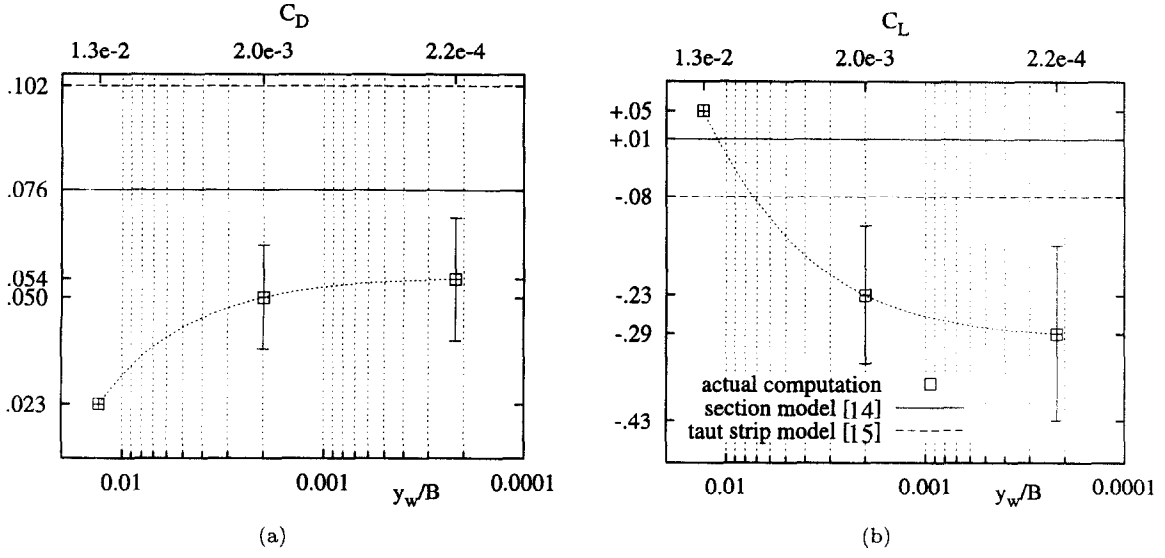

Figure 9. Effects of grid spacing on aerodynamic coefficients.

The mean value of the drag coefficient increases consistently with the shear-layer separation and the vortex shedding around the deck. In particular, the drag component involved in the flow circulation in the near-wake area is generally predominant in such quasibluff geometries.

In order to relate the drag value and the characteristics of the wake, Figure 10 presents the effect of grid spacing on the across-wind extent of the wake and on the velocity defect at two locations in the wake ($0.005B$ and $0.5B$ from the trailing edge). The coarsest grid does not predict any recirculation, so that the deck behaviour is close to the one of a fully streamlined section and is characterized by a very low drag value. The profiles predicted using the other models are quite similar. The model lam-3 further reduces the velocity defect in the neighbourhood of $y/B = 0$ and emphasizes the wake extent in the range $-0.2 < y/B < -0.1$ because of the wider separation bubble at the lower surface of the deck. It may be noted that the results are in good agreement with the computational prediction of Larsen [18] using DVM. Even though the $\bar{C}_D$ value approaches the section-model result, it remains somewhat underestimated. This is certainly due to the absence of deck equipment in the models.

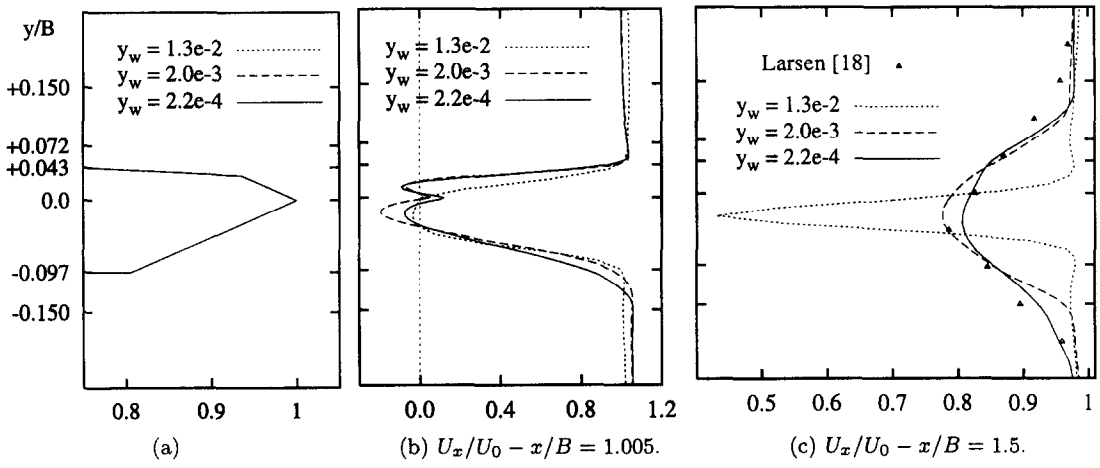

Figure 10. Effects of grid spacing on mean x-velocity defect in the wake.

Instead, mesh refinement considerably reduces the lift forces acting on the deck. It may be noted that as the grid spacing becomes smaller, the computed $\bar{C}_L$ moves out of the range of the measured values, and its standard deviation increases. Hence, mesh refinement enables a qualitative reproduction of the vortex-shedding process but also appears to reduce accuracy in predicting the mean lift force. The same apparent discrepancy may be noted in other 2D simulations (e.g., [21]; see Table 1). Even though Kuroda assumed the same grid spacing near the wall, the error regarding the lift coefficient is somewhat different from the present results. This difference points to the dependence of numerical damping both on grid spacing and on the convective scheme. To clarify this aspect, the levels of performance of the finest grid are evaluated in the case where second-order upwind and QUICK schemes are employed.

The distributions obtained for the mean Cp and for the std (Cp) are compared in Figure 11. The agreement between the lift coefficient measured and the lift coefficient obtained from the "y_w = 1.3e − 2-2nd upw" model is seen to be merely fortuitous. From a comparison of the unsteady solutions it is found that as the mesh becomes more refined and the order scheme is higher, the diffusion effect is progressively reduced and does not overcome the very small viscous diffusion of the flow. Hence, the extent of the separation bubble at the lower surface is shortened, and the separated layer past the upper leading edge is better predicted. Despite the major gain in precision that is obtained, the size of the separation bubbles remains somewhat larger than the measured value.

Two main limitations remain in 2D laminar simulations. First, it is clear that further refinements of the near-wall mesh or the adoption of higher-discretization schemes do not represent

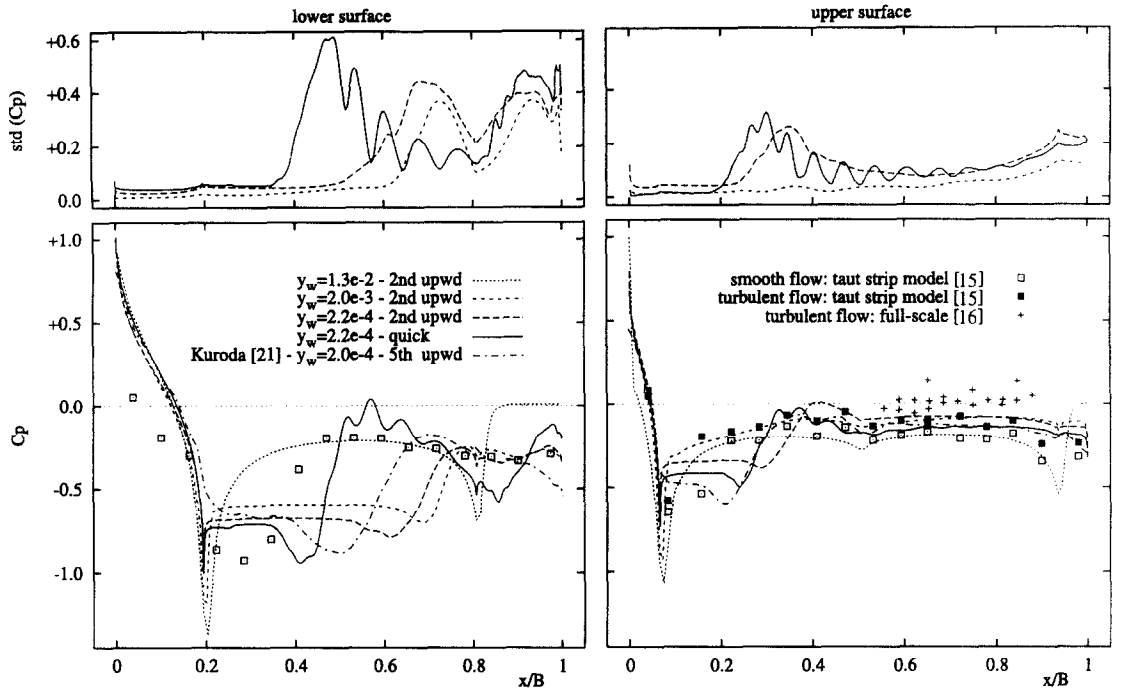

Figure 11. Effects of numerical diffusion on mean Cp and std (Cp) distributions.

realistic solutions. In fact, the evolution of the aerodynamic coefficients versus near-wall cell thickness (see Figure 9) seems to indicate that further refinement does not bring about any significant improvement. On the other hand, the reduction of numerical damping by the highest diffusive schemes is such that wiggles appear (see Figure 11 "$y_w = 2.2\text{e}-4$-QUICK" model), and the stability of the computations seems to be no longer assured. Second, the failure to model 3D effects remains. In particular, the well-known diffusion in the spanwise direction and the energy-transfer mechanism towards higher frequencies as a result of vortex stretching [7] continue to be neglected.

4.2. Statistical Approach

The most refined grid selected in the laminar simulations is retained in the sequel of the present paper. The grid spacing near the wall complies with the requirements for correct application of the two-layer model (wall unit $y^+ \approx 1$). Table 4 summarizes the main integral parameters obtained by applying the standard $k-\varepsilon$ model (STD), the RNG model and the Reynolds stress model (RSM). Both the STD and RNG models fail to predict the unsteadiness of the flow. This error can no longer be chiefly put down to the numerical damping that results from the combined effect of grid size and discretization scheme on account of the previous optimization. It follows that the reasons for the lack of lift fluctuations (std $(C_L) = 0$) are to be sought rather in the formulation of the turbulence models adopted.

Table 4. Statistical approach: integral parameters.

Model	$\bar{C}_D$	$\bar{C}_L$	std (C_L)	St
Reinholds [14]	0.08	0.01	–	0.109 – 0.158
Larose [15]	0.10	– 0.08	–	0.11
STD	+ 0.043	– 0.067	0.0	steady
RNG	+ 0.043	– 0.008	0.0	steady
RSM	+ 0.058	+ 0.026	0.0073	0.289

Recently, Shimada and Ishihara [3] have proposed an interesting explanation of the severe limitations of these models in correctly simulating the fluctuating pressure field around elongated rectangular sections. Franke and Rodi [31] argue that in vortex-shedding flows an instantaneous quantity ϕ can be separated into

$$\phi(t) = \bar{\Phi} + \underbrace{\tilde{\Phi} + \phi'}_{\Phi'}. \tag{14}$$

Indicating by Φ' the total fluctuation (i.e., periodic $\tilde{\Phi}$ plus stochastic ϕ') around the time-mean value $\bar{\Phi}$, its variance can be expressed as

$$\sigma^2_{\Phi'} = \sigma^2_{\tilde{\Phi}} + \sigma^2_{\phi'}. \tag{15}$$

In particular, the above equation (15) can be rewritten for the velocity component U_i as follows:

$$\sigma^2_{U_i'} = \underbrace{\frac{1}{T}\int_0^T \tilde{U}_i{}^2(t)\,dt}_{\sigma^2_{\tilde{U}_i}} + \underbrace{\nu_t S_{ij} - \frac{2}{3}k\delta_{ij}}_{\sigma^2_{u_i'}}. \tag{16}$$

The stochastic component of the velocity is evaluated by means of the turbulent kinetic energy k and then related to the turbulent viscosity ν_t. It follows that the value of the variance strictly depends on the reliability of one of the weakest and most debatable assumptions of the model, namely, the isotropic turbulent viscosity itself. Furthermore, the stochastic component of the pressure is not explicitly modelled in any RANS model, so that

$$\sigma^2_{P'} = \sigma^2_{\tilde{P}} + \sigma^2_{p'} > \sigma^2_{\tilde{P}} = \sigma^2_{P',\mathrm{RANS}}$$

and

$$\mathrm{std}\,(\mathrm{C_L})_{\mathrm{RANS}} < \mathrm{std}\,(\mathrm{C_L}).$$

The statistical approach yields good results in the case of massively separated flow in which periodic fluctuations predominate. These conditions do not apply to the present application, where the relative contribution of the stochastic component becomes noticeable. Moreover, in this case the very small eddies observed without turbulence modelling are probably assumed in the stochastic field by the statistical approach. As a result, these models yield higher levels of eddy viscosity around the deck and in the wake. This may damp the fluctuating motion to such an extent as to cause the observed lack of unsteadiness.

The RSM model furnishes an unsteady solution, even though one characterized by an extremely reduced value of the standard deviation of the lift coefficient and a unique Strouhal number (Figure 12a). This frequency content is due to the single eddy in the wake of the deck (Figure 12b).

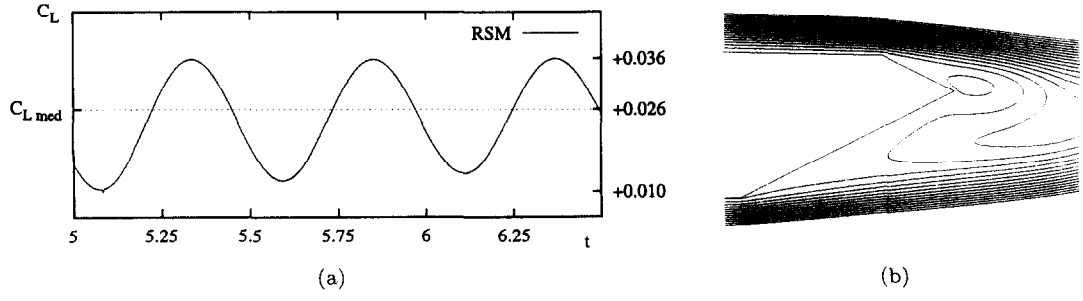

Figure 12. RSM-time history of lift coefficient (a) and instantaneous streamlines (b).

As a result, the RSM model affords scant improvement in the simulation of the flow as compared to the two-equation closure. This is probably due to the formalism adopted by Lien and Leschziner [34] for modelling the turbulent-diffusion term

$$D_{ij}^{T} = \frac{\partial}{\partial x_k}\left(\frac{\nu_t}{\sigma_k}\frac{\partial \overline{u_i u_j}}{\partial x_k}\right).$$

In fact, the above approach is once more based upon the concept of isotropic turbulent viscosity ν_t, and the value of the free constant $\sigma_k = 0.82$ is obtained by applying the generalized gradient-diffusion model to a case that is rather different from the present one, i.e., a plane homogeneous shear flow.

4.3. The Large Eddy Simulation Approach

The adoption of the LES approach, albeit somewhat burdensome, is necessary to overcome the substantial difficulties involved in simulating the turbulent flow around the GBEB deck using the statistical approach.

4.3.1. Optimization of computational parameters

The effects of two computational parameters are investigated in what follows, namely, the interval for time advancement Δt and the discretization scheme for the convective terms.

Table 5 summarizes the main integral results obtained by varying the above-mentioned parameters; the bold style highlights the particular parameters that change. The results obtained using the models les-1 and les-2 do not significantly differ from one another. It follows that the largest time step is still smaller than the characteristic time of the smallest vortex directly simulated by the mesh adopted. On the other hand, the increase in Δt markedly reduces the number of iterations required at each step (-40%) to reach convergence (threshold for residuals fixed at $5.e-4$). For this reason the value $\Delta t = 1.e-2$ is adopted in the subsequent simulations.

Table 5. Computing conditions and integral parameters.

Model	Δt	Scheme	C_s	$\bar{C}_D$	$\bar{C}_L$	std (C_L)	St
les-1	**1.e−3**	2nd up	0.10	+0.067	−0.301	0.148	0.272 – 0.113
les-2	**1.e−2**	**2nd up**	0.10	+0.066	−0.307	0.140	0.272 – 0.107
les-3	1.e − 2	**QUICK**	0.10	+0.075	−0.164	0.179	0.202 – 0.101
les-4	1.e − 2	**2nd cnt**	0.10	+0.071	−0.195	0.168	0.124 – 0.164
							0.197 – 0.292

In a way similar to the one adopted for simulations without turbulence models, the remaining part of this subsection is devoted to clarifying the performance of various discretization schemes in conjunction with LES and to selecting the most efficient scheme for the ensuing runs. As compared to the second-order upwind scheme, the QUICK scheme enables the fluctuations of the lift force to be increased and the mean computed value of the lift force to be brought closer to the experimental data. This trend is clarified by the distribution of the mean pressure coefficient and the distribution of its standard deviation in Figure 13.

The differences between the QUICK scheme and the second central scheme are less marked, at least as regards the mean Cp distribution at the lower surface of the deck. However, the separation bubble at the upper surface is only detected by the second central scheme, even though the suction remains somewhat underpredicted. Another two characteristics of the simulated flow argue in favour of the latter convective scheme.

The first is the transverse extension of the wake downstream of the deck (see Figure 14a). The profiles obtained from applying the second upwind scheme and the QUICK scheme do

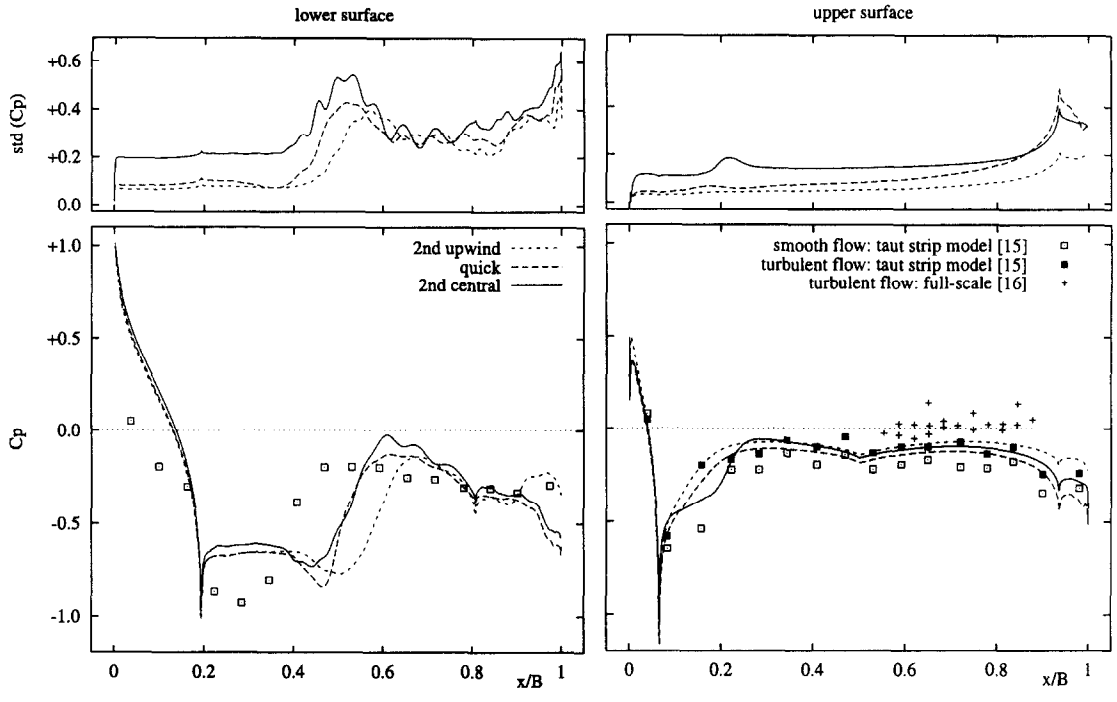

Figure 13. Cp and std (Cp) distributions on the deck.

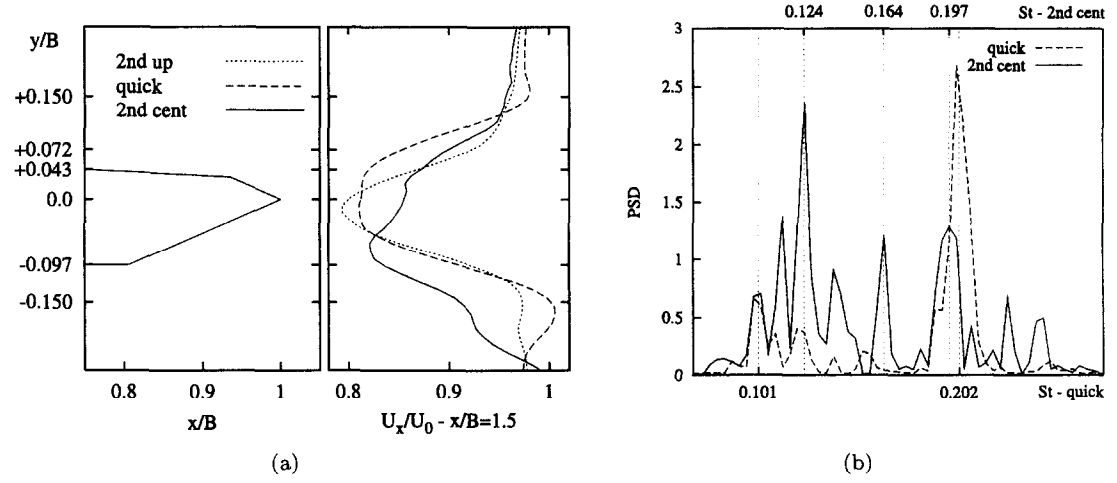

Figure 14. Mean x-velocity defect in the wake (a); Strouhal number (b).

not substantially differ from one another. Instead, the second central scheme emphasizes the contribution of the vortices v_1 to the velocity defect.

The frequency content of the lift force predicted by means of the second central scheme (see Table 5 and Figure 14b) is spread over a wider range ($0.1 \leq \mathrm{St} \leq 0.2$) than the one predicted by the other schemes. This result is hardly surprising if the dispersive effect of the odd-order leading term is borne in mind. Furthermore, the main Strouhal number in the second central simulation is the lower one ($\mathrm{St} = 0.124$), which is related to merging between the vortices at the lower surface and at the leeward edges. Instead, the upwind schemes attribute most of the energy to the higher shedding frequency ($\mathrm{St} \approx 0.2$), which is exclusively due to the vortical structures emerging at the leading edge.

All the above-mentioned characteristics are due to the smaller numerical diffusivity related to the second-order central scheme, and thus, to its capability for describing the effect of the small vortical structures at the lower surface of the deck. For these reasons, the second-order central

scheme seems to be the most adequate one for the present application. This result confirms the conclusions reached by Breuer [42] concerning the numerical effects on large-eddy simulation in the case of flow past a circular cylinder.

4.3.2. Effects of the Smagorinsky constant

The subgrid model developed by Smagorinsky introduces only one free input parameter, namely, the so-called Smagorinsky constant C_S. Consequently, the arbitrariness of the model is substantially reduced as compared to the statistical approach (five semiempirical constants are required in the standard $k-\varepsilon$ model). However, the Smagorinsky constant plays a very important role in LES because its value may considerably affect the turbulent viscosity.

The value of C_S has been optimized by several authors in the case of 3D simulations and has generally been set at $C_S = 0.1$. On the other hand, it is our opinion that the optimization of the subgrid model has not been taken into due consideration in 2D simulations.

Generally speaking, the presence of a subgrid model makes a substantial difference with respect to direct numerical simulation and potentially enables application of the LES approach to 2D simulations in the case of homogeneous spanwise fluctuations. In particular, an adequate tuning of the free parameter of the subgrid model could enable reproduction of the characteristic effects of the vortical structures generally observed in 3D configurations [8]. In order to verify

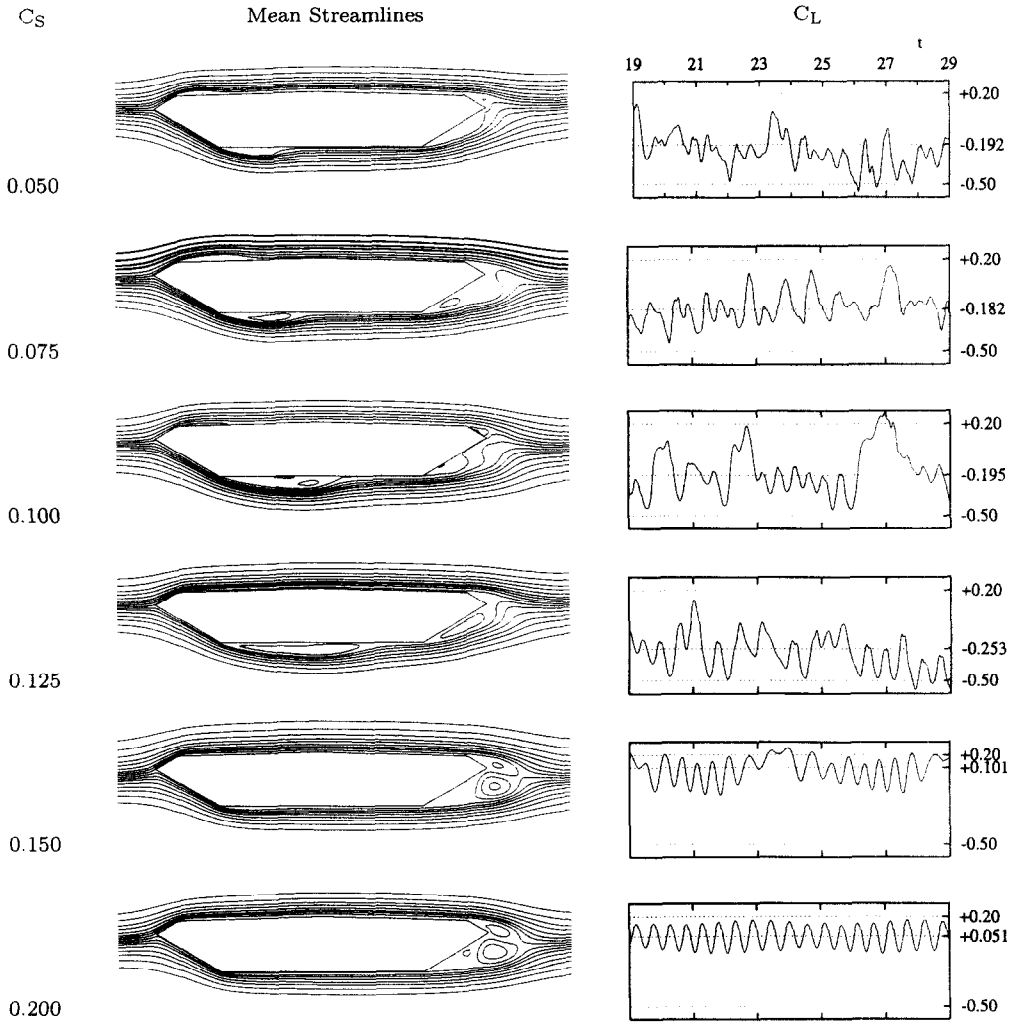

Figure 15. Time histories of C_L and mean streamlines.

the advisability of such a procedure, a number of values of the Smagorinsky constant in the range $0.05 \leq C_S \leq 0.2$ were tested for the present case study.

Figure 15 compares the time histories of the lift coefficient in the range $19 \leq t \leq 29$ and the mean streamlines obtained by applying a selected number of C_S values. The value $C_S \approx 0.1$ represents a watershed for the quantities examined.

As the value of the Smagorinsky constant exceeds 0.1–0.125,

(i) the separation bubble at the lower surface is abruptly reduced ($0.125 \leq C_S \leq 0.15$);
(ii) the merging of the vortices v_1 and v_2 (see Figure 1) vanishes;
(iii) the mean value of the lift coefficient increases;
(iv) the oscillations of the the lift coefficient diminish; and
(v) the time history of the lift coefficient approaches a perfect sinusoid ($C_S = 0.2$).

Instead, as the value of the Smagorinsky constant becomes smaller than 0.125–0.1, the evolution previously observed is not altogether respected. In particular,

(i) the length of the separation bubble at the lower surface gradually reduces ($0.05 \leq C_S \leq 0.125$);
(ii) the recirculating zone downstream of the upper windward edge appears;
(iii) the mean value of the lift coefficient increases;
(iv) the fluctuations of the lift coefficient diminish; and
(v) the frequency content of the lift coefficient appears to spread over a larger range in the direction of the higher frequencies.

To provide a better description of these trends and to clarify the reasons behind them, the step in the variation of the value of C_S is further reduced. The evolution of the drag and lift

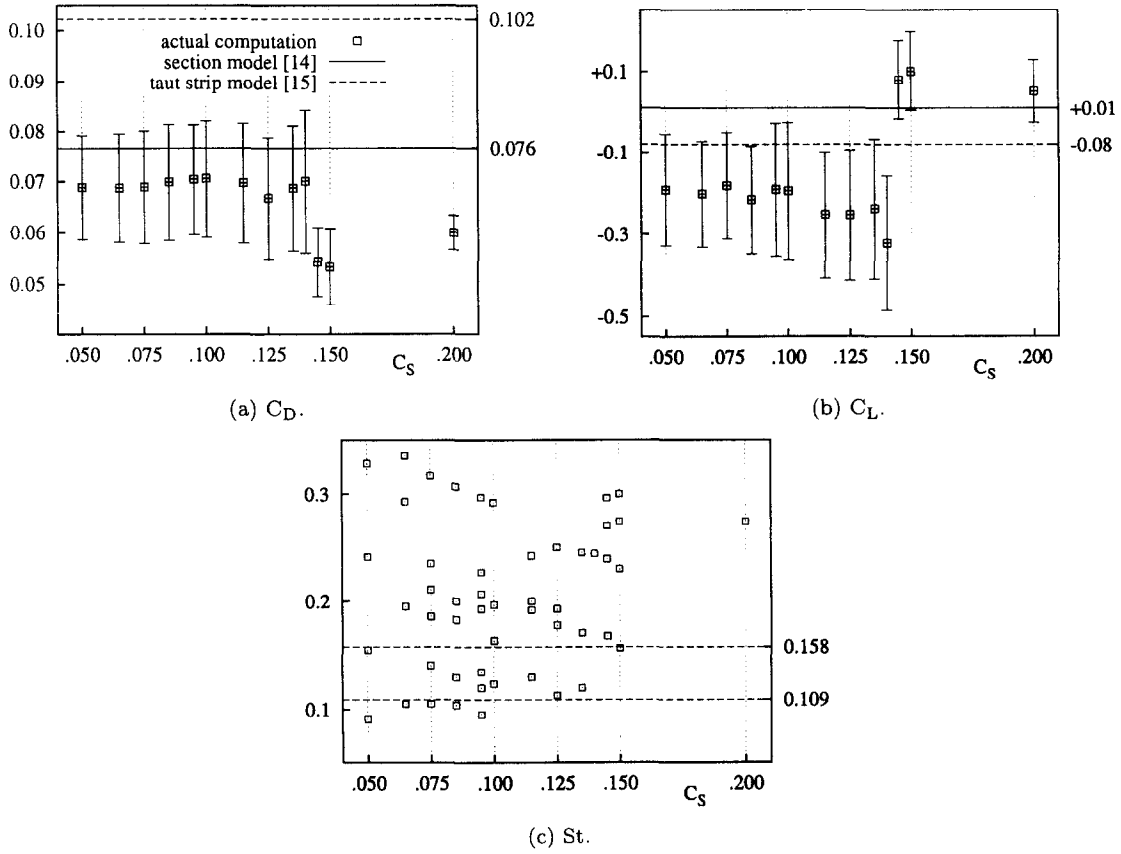

(a) C_D. (b) C_L.

(c) St.

Figure 16. Effects of C_S on the aerodynamic coefficients and on the Strouhal numbers.

coefficients and of the Strouhal numbers versus the Smagorinsky constant are plotted in Figure 16. The discontinuities in the evolutions of C_D and C_L evolutions clearly appear at $C_S \approx 0.145$, so revealing a significant case sensitivity to this parameter. At the lowest values of C_S the aerodynamic parameters present the best agreement with the experimental measurements. The evolution of the Strouhal numbers is obtained by evaluating the reduced frequencies corresponding to the main peaks in the PSD of the lift force for each simulation. The diagram confirms that as the value of C_S decreases, the frequency content is more spread out and the upper bound of the range increases. Consistently with the diagrams of the aerodynamic coefficients, for $C_S > 0.140$ the simulated Strouhal numbers do not at all match the values measured in wind-tunnel tests. Once again, the best agreement is obtained in the range $0.075 < C_S < 0.095$.

The mean Cp distribution on the deck surface in Figures 17 and 18 makes it possible to identify the reasons for the aforesaid variation in the global aerodynamic behaviour of the deck and to schematically delineate three main ranges for the C_S value.

In the upper range ($0.2 \leq C_S \leq 0.145$) the flow is fully attached to the wall of the deck, and no significant fluctuations of the pressure can be observed. Low values of the drag coefficient and positive lift forces characterize the aerodynamic behaviour of the deck. The unsteadiness of the flow is exclusively due to the vortices emerging at the downstream corners. The vortices are shed at high frequencies, and the interaction between eddies is restricted to the upper and lower ones in the near wake.

At values of the Smagorinsky constant in the range $0.140 \leq C_S \leq 0.115$, the separation bubble at the lower surface is predicted even though its length is largely overestimated. For $C_S = 0.140$ the value of std (Cp) is very low at $x/B = 0.8$, which indicates that there is not yet any interaction between the vortices v_1 and v_2. As the value of the Smagorinsky constant is further reduced, interaction is set up and increases progressively; however, if we examine the Strouhal numbers we find that vortex merging does not yet represent the main mechanism in vortex shedding. The flow at the upper surface still remains attached to the wall. The drops in the pressure distributions, again on the upper surface, can be explained by considerations that regard the

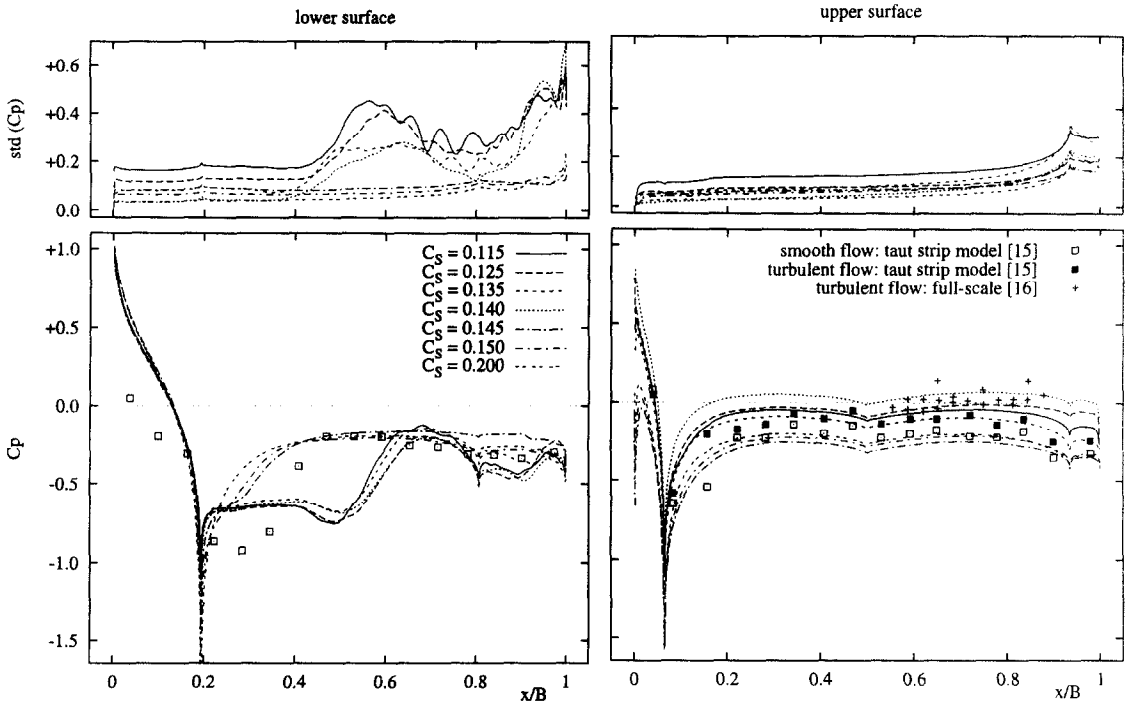

Figure 17. Cp and std (Cp) distributions on the deck—$C_S \geq 0.1$.

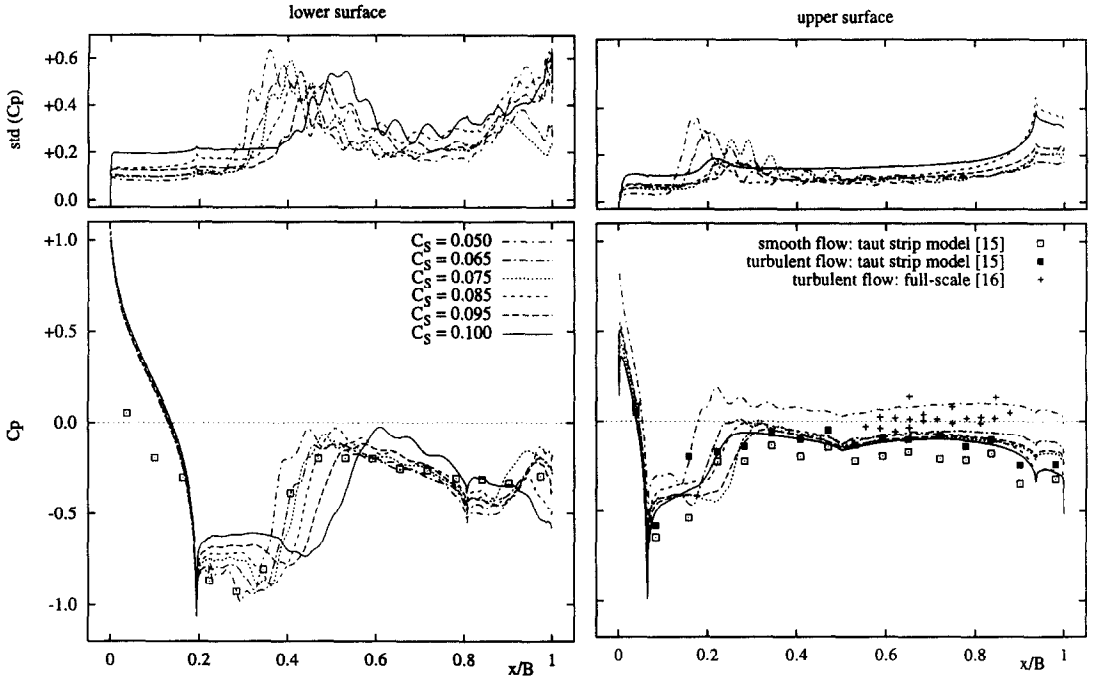

Figure 18. Cp and std (Cp) distributions on the deck—$C_S \leq 0.1$.

energy conservation of the flow. Finally, as the Smagorinsky constant is reduced from $C_S = 0.1$ to $C_S = 0.05$, the suction at the lower surface diminishes so much that it matches the experimental measurements. On the upper surface, the flow is separated past the leading edge. Three main subranges of shedding frequencies may be identified: the first range corresponds closely to the experimental one ($0.11 < St < 0.16$); the second range ($St \approx 0.2$) remains quite constant as C_S varies in the range $0.05 < C_S < 0.1$; the upper bound of the third range constantly increases as C_S decreases.

From an overall analysis of the above results, it is possible to interpret the effects of the Smagorinsky constant. The results observed for $C_S > 0.1$ are hardly surprising if we bear in mind the expression of the subgrid-scale eddy viscosity ν_{SGS} (equations (9) and (10)). As the Smagorinsky constant increases, the subgrid eddy viscosity is progressively overestimated, and its diffusion effect obscures the small-scale eddies at the root of the unsteadiness of the flow. It should be pointed out that the effects of the Smagorinsky constant in this range of values are similar to the effects of the numerical diffusion due to the grid spacing and the discretization schemes investigated above.

For $C_S < 0.1$, the subgrid eddy viscosity is progressively underestimated. As a result, not only the diffusive effects fail to conceal the small eddies but also higher frequency fluctuations are introduced in the 2D simulation. The spectrum of the 2D computations, which is generally confined within a narrow band [7], is artificially extended over a wider band. This obviously leads to the above-mentioned higher Strouhal number, but also affects the energy-transfer mechanism. In fact, in 3D simulations a number of three-dimensional features of the flow (such as, vortex stretching and longitudinal eddies in the wake) play an important role in the energy cascade, subtracting an important amount of energy from the transverse flow. Of course, these energy-transfer mechanisms cannot be simulated exactly in 2D analysis, but their overall effects can be replaced by a reduced value of the Smagorinsky constant. On the other hand, this approach introduces into the flow field a number of small-sized high-frequency disturbances (wavelets) clearly revealed by the distribution of the mean pressure coefficient (see Figure 18, in particular for $C_S = 0.05$). In this sense, the effects of the smallest value of C_S are similar to those involved in the numerical dispersion of certain discretization schemes.

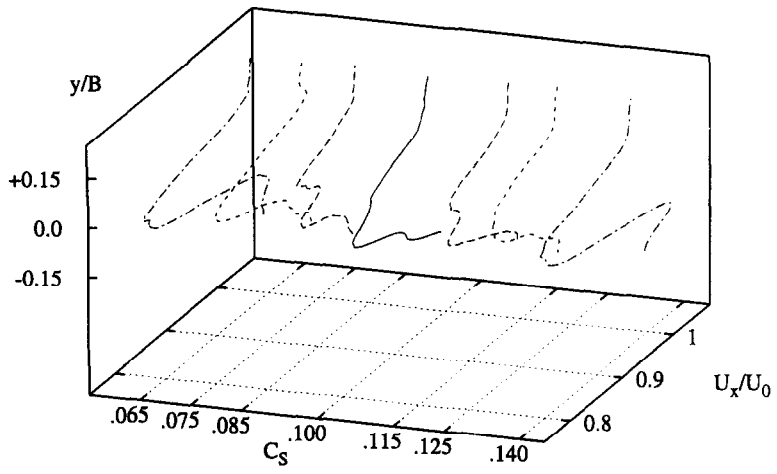

Figure 19. Effects of C_S on the mean velocity defect in the wake $x/B = 1.5$.

The evolution of the mean velocity defect in the wake at $x/B = 1.5$ versus the Smagorinsky constant (see Figure 19) would seem to confirm the above explanation. The wake reaches its maximum across-wind extension at $C_S = 0.1$, i.e., when the flow energy is neither diffused by an excessive amount of subgrid eddy viscosity ($C_S > 0.1$) nor dispersed in a wider band spectrum ($C_S < 0.1$). In particular, both phenomena have the same effect on the mean velocity in the wake, as emerges from the correspondence between the curves.

From the results obtained it follows that a C_S value in the range $0.65 < C_S < 0.75$ is more suitable in 2D simulations for the case study. However, the simplified geometry of the deck does not enable a final verdict to be issued. On the one hand, the small number of nodes obtained by neglecting the barriers has made possible a number of extended and useful parametric studies. On the other hand, the failure to meet the experimental conditions for the equipment does not enable a direct comparison with the experimental data, a complete validation of the approach here proposed or a clear singling-out of the effects of the barriers on the physics of the flow.

4.4. Effects of Deck Equipment

In order to overcome the above-mentioned difficulties, in what follows the deck equipment is introduced into the model. The close-up view of the mesh generated around the fully equipped section is shown in Figure 20b. The near-wall cell thickness is set at $y_w = 3.1\mathrm{e}-4B$. Modelling of the barriers involves an important increase in the number of cells (76564, +68% as compared to the lam-3 grid). To enable an appreciation of the computational resources involved, Figure 20a summarizes the evolution of CPU time versus cell number in LES simulations (HP j6000-1 proc. PA8600 552 MHz, SPECfp2000 433). The 2D detailed model (11 days for a computer run involv-

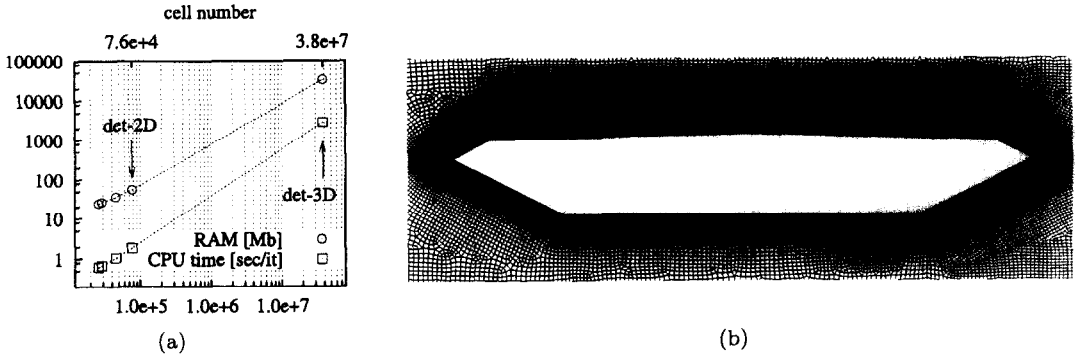

Figure 20. CPU time versus cell number (a); grid system near the detailed deck (b).

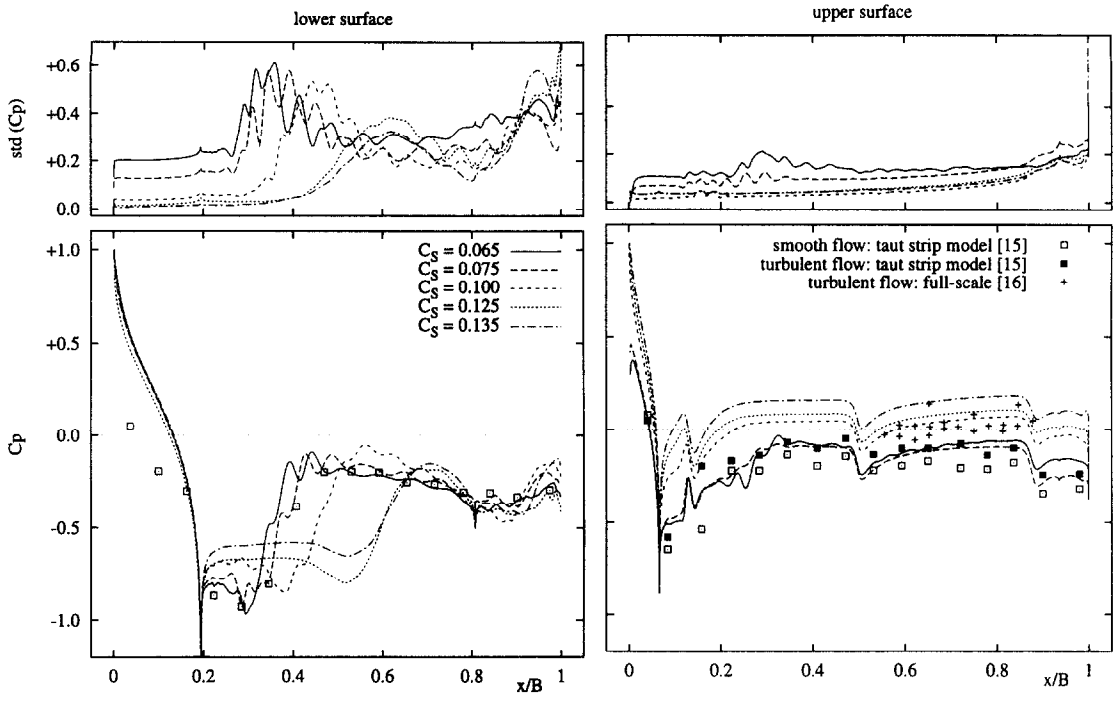

Figure 21. Effects of C_S on Cp and std (Cp) distributions on the detailed deck.

ing 5000 time steps) is certainly more time-consuming than the basic one (six days). It follows that the advisability of introducing deck equipment must be carefully evaluated against the gain in accuracy. On the other hand, the extension of the same grid system in the spanwise direction (3D simulation, spanwise dimension of the computational domain set at 1 chord length B) markedly increases the required computational resources (CPU time of 44 years). It is evident that such a computational commitment is out of the question in the case of parametric studies or industrial applications. The above data confirm the importance of developing computational approaches alternative to 3D simulations in these fields.

First of all, the parametric study on the effect of the Smagorinsky constant in 2D-LES computations is applied to the detailed deck in order to detect with a greater degree of precision the optimal C_S value for the case study. The analysis is restrictedly performed on the most suitable values of C_S previously selected in the basic simulations.

Figure 21 shows the distribution of the mean pressure coefficient and the distribution of its standard deviation on the deck. The effects of the Smagorinsky constant previously observed in the basic geometry (see Figures 17 and 18) is generally confirmed. However, the results in some crucial areas of the deck indicate that the value $C_S = 0.075$ is the most suitable one. In fact, at $C_S = 0.065$ the length of the recirculating area on the lower surface is underestimated, and instabilities increase behind the barriers at the upper surface. The disagreement between the experimental measurements and the computational results remains at the lower surface in the range $0 < x/B < 0.2$. If it is borne in mind that the anisotropy of the turbulence in the forebody region is probably the cause of this disagreement, it is hardly surprising that the Smagorinsky subgrid scale model proves its insufficiency.

The models that yielded the most satisfactory results in the previous simulations (namely, the laminar approach, the Reynolds stress model, and the large eddy simulation with $C_S = 0.075$) are applied in what follows to the detailed deck. Table 6 compares the main integral parameters of the flow resulting from models with and without barriers.

The results obtained using the RSM model are of less interest than the validation of the computational approach and do not provide a significant physical insight into the flow. Nevertheless,

Table 6. Integral parameters with and without barriers.

Model	$\bar{C}_D$	$\bar{C}_L$	std (C_L)	St
Reinhold [14]	0.08	0.01	–	$0.109 \leq St \leq 0.158$
Larose [15]	0.10	−0.08	–	$St = 0.11$
rsm-bas	+0.058	+0.026	0.007	$St = 0.289$
rsm-det	+0.077	−0.035	0.001	$0.216 \leq St \leq 4.68$
lam-bas	+0.054	−0.288	0.139	$0.094 \leq St \leq 0.186$
lam-det	+0.080	−0.387	0.124	$0.080 \leq St \leq 0.227$
les-bas	+0.069	−0.182	0.130	$0.105 \leq St \leq 0.317$
les-det	+0.086	−0.199	0.123	$0.098 \leq St \leq 0.333$

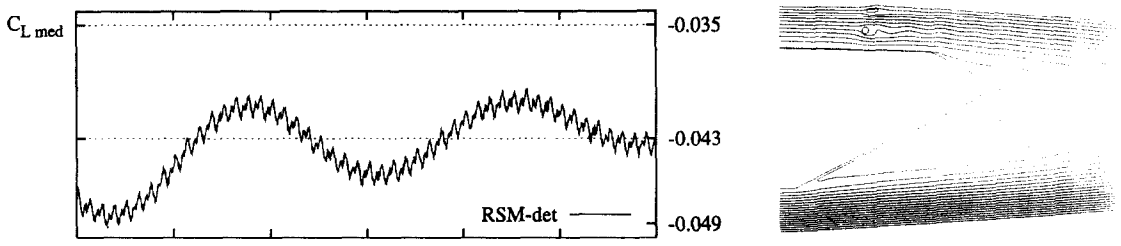

Figure 22. RSM model: time track of lift coefficient (a) and instantaneous streamlines (b).

they are briefly commented upon in what follows in order to confirm the hypothesis formulated regarding the weakness of the statistical approach. As in Figure 12, Figure 22 shows the time history of the lift coefficient and the close-up view of the instantaneous streamlines in the near-wake region. The computational solution is characterized by a transient phase (see Figure 22a), in which the low-frequency fluctuations of the lift force are due to vortex shedding in the wake of the deck. These fluctuations progressively vanish, and only the high-frequency ($St = 4.68$), small-amplitude ($\text{std}(C_L) = 0.001$) fluctuations remain in the stationary solution. The final unsteadiness of the flow is exclusively due to vortex shedding downstream of the leeward side barriers, as shown in Figure 22b. Once again, the statistical approach proves its capability for detecting only periodic phenomena. The stochastic perturbations from the ensemble-averaged fluctuation-such as the perturbations induced by small-scale, complex eddies-are assumed in the turbulent field. It follows that the eddy viscosity considerably increases and progressively dissipates the periodic fluctuation.

The comparison of the results obtained from the laminar and LES approaches makes it possible to highlight the differences related to flow modelling, as well as the common trend that results from barrier modelling. As may be readily appreciated from Table 6, the main effects of the equipment on the aerodynamic coefficients may be summarized as follows:

(a) rise in the drag force;
(b) drop in the mean value of the lift force and its fluctuations;
(c) wider band of the lift spectrum (St).

A previous work [12] has demonstrated that the contribution of small-sized items of equipment to bridge aerodynamics is primarily due to interference effects between the items of equipment and the deck. In what follows, these interference phenomena will be further distinguished as local effects (i.e., regarding the neighbourhood of the items of equipment) and global effects.

As for the mean drag coefficient, the increase in its value due to the barriers is approximately the same in both the laminar and LES approaches ($\Delta C_D \approx 30\%$). Such a major increase cannot be related to the direct contribution due to the details. Instead, we shall focus our attention on the contribution of the base region of the deck.

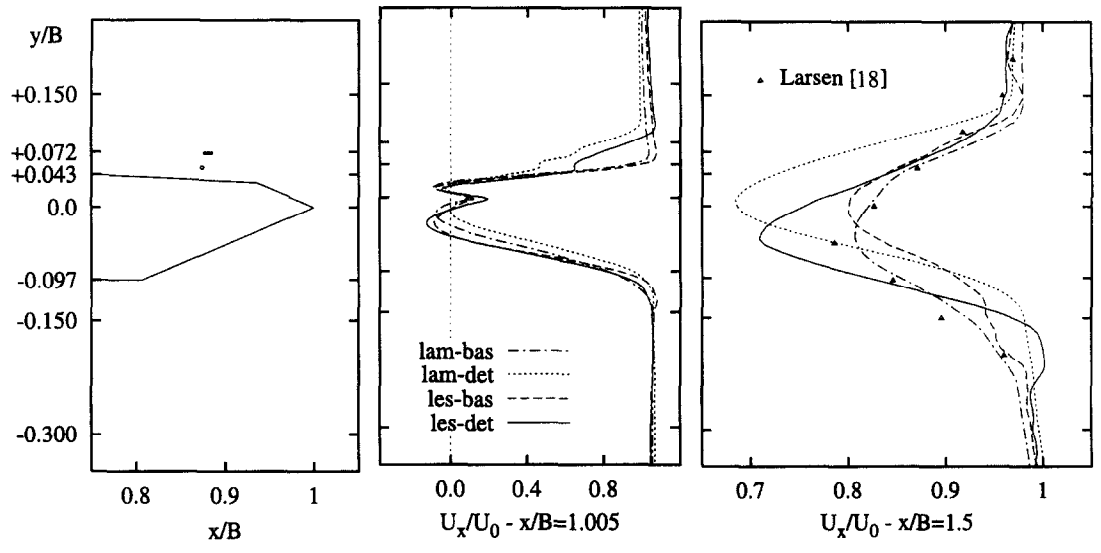

Figure 23. Velocity defect in the wake: basic and detailed deck.

Figure 23 shows the mean velocity defect along two straight lines at different locations in the wake. The details increase the ratio between the width of the wake at $x/B = 1.005$ and the width of the deck. As a result, the distance between vortices of different sign is augmented, and the deck experiences a higher drag value, which closely matches the experimental data. In this sense, the presence of the details increases the overall degree of bluffness of the section.

Finally, it is to be pointed out that the introduction of the barriers in the laminar and LES approaches leads to rather different predictions of the abscissa of the local maximum defect along the straight line at $x/B = 1.5$. In the laminar simulations the velocity defect due to the barriers is not diffused along the wake, and the local velocity minimum is aligned with the upper surface. Instead, in LES the modelling of the barriers involves a downturn of the local velocity minimum and a less regular profile of the mean velocity U_x. The above phenomenon would appear to have the same cause as the reduction in the lift coefficient and in the lower bound of the Strouhal range.

In order to provide a comprehensive explanation of the above results, the mean profiles of the longitudinal component of the velocity U_x and of the vorticity ω along the straight line $x/B = 0.328$ are shown in Figure 24. The profile of the mean longitudinal velocity over the upper surface ($y/B > 0.039$) in Figure 24b confirms that the velocity defect in the wake is due to the barriers, which also shed a certain amount of vorticity in their wake (Figure 24c).

The most surprising results concern the lower side area. On account of the blockage effect of the upwind side barriers, the velocity increases over the lower side of the deck as compared to the case of the basic geometry (see Figure 24d). As the velocity U_s outside the outer boundary layer at the separation point increases, the instantaneous flux of vorticity also increases according to the relation

$$\frac{d\omega}{dt} = \frac{1}{2}\left(U_s^2 - U_b^2\right),$$

where U_b is the corresponding velocity from the base to the same point. Hence, the vorticity shed downstream of the separation bubble is higher and more concentrated (see Figure 24e). Consequently, the vorticity, convected along the lower surface of the deck, moves downstream of the maximum velocity defect in the wake. Furthermore, the increased velocity of the flow involves a deeper suction on the lower surface of the deck (see Figure 25) both in the laminar simulation ($0.55 < x/B < 0.65$) and in the LES simulation ($0.2 < x/B < 0.4$). The more concentrated vorticity reduces the length of the separation bubble and enables the LES simulation to make a correct prediction of the experimental pressure distribution. Both phenomena are indirectly

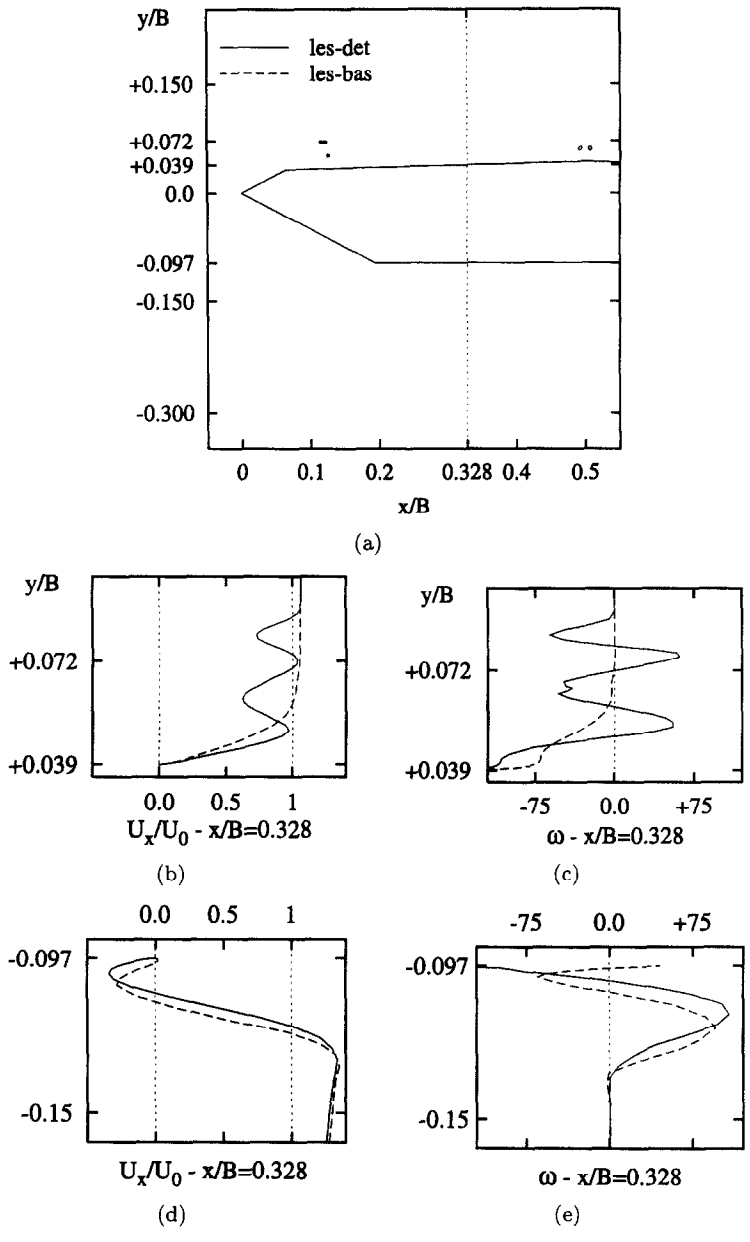

Figure 24. Effects of C_S on the aerodynamic coefficients and on the Strouhal numbers.

involved by the barriers and contribute to reducing the value of the lift coefficient. Of course, the barriers also have local effects on the upper surface, which involve local maxima and minima in the pressure distribution. In particular, the upwind side barrier reattaches the flow past the upwind edge, reducing the pressure fluctuations predicted in the basic configuration (see the std (C_p) distribution on the upper surface). The mean streamlines in Figure 26a confirm both the local and the global effects.

Finally, the barriers also affect the mechanism of the vortex-formation process and the Strouhal numbers. Once again it is possible distinguish direct (i.e., local) phenomena and interaction (i.e., global) phenomena. The former effects can be identified in the classical Karman vortex streets in the wake of the circular barriers. This kind of shedding is probably responsible for the higher frequency content of the lift force (see Figure 26b) in the detailed configuration (St from 0.317 to 0.333). However, somewhat surprisingly the barriers also affect the lower bound of the Strouhal number range, namely, the shedding frequency related to the interaction between the

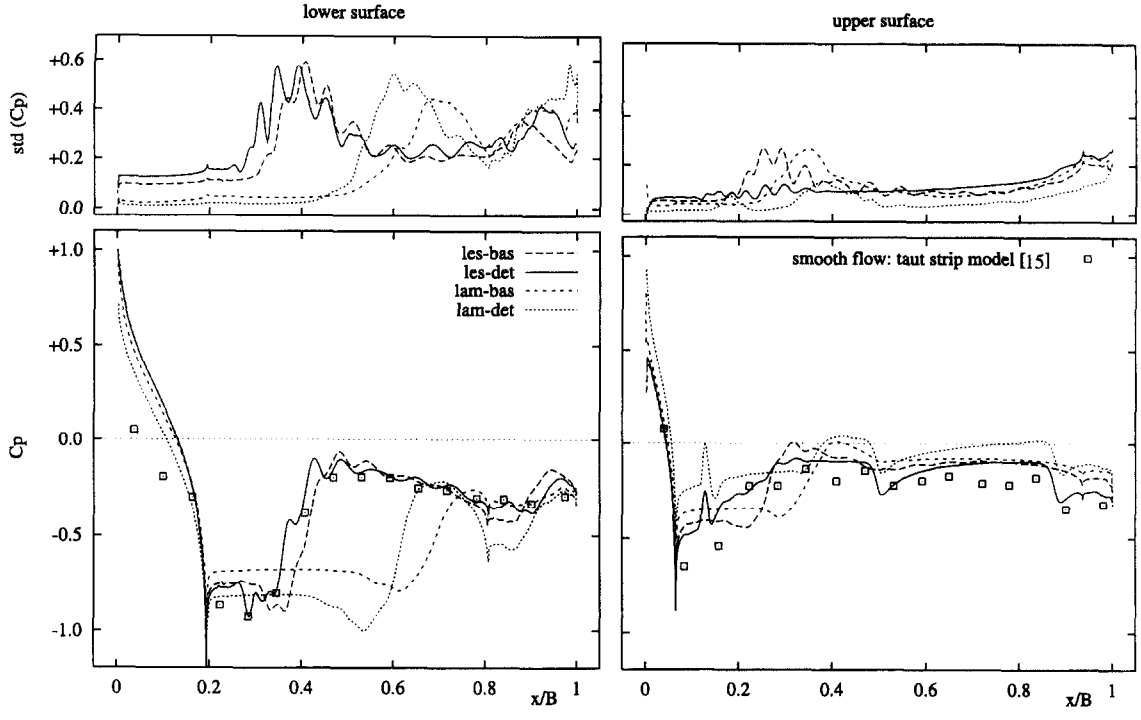

Figure 25. Cp and std (Cp) distributions on the basic and detailed deck.

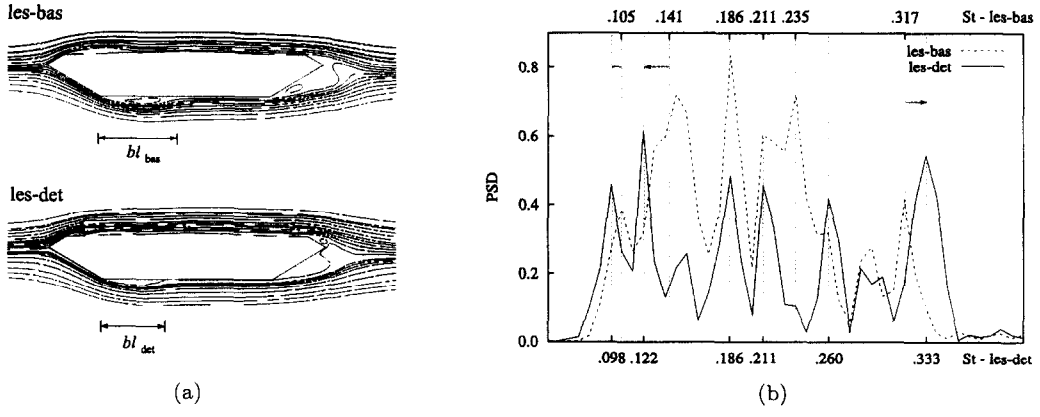

Figure 26. Mean streamlines (a) and frequency content of C_L (b): basic and detailed deck.

vortices v_1 that are shed from the separation bubble and the vortices v_2 that emerge past the leeward edge. As a result of the reduction in the length of the bubble bl_{det} (see Figure 26a), the vortices v_1 translate along a greater length to reach the leeward edge and to merge into the vortices v_2. Thus, the shedding period becomes longer and the associated Strouhal number is reduced from $0.105 \leq \text{St} \leq 0.141$ (without barriers) to $0.098 \leq \text{St} \leq 0.122$ (with barriers).

4.5. Flow Around the Deck with Angle of Attack

The goal of the simulations presented herein is to provide a further validation of the proposed 2D approach based upon the modified value of the Smagorinsky constant $C_S = 0.075$.

The aerodynamic behaviour of the GBEB deck has been experimentally investigated at various angles of attack. The mean pressure distribution on the deck measured in the wind-tunnel tests by Reinhold *et al.* [14] is available in the literature [25] for an incidence of 6 degrees (wind from below).

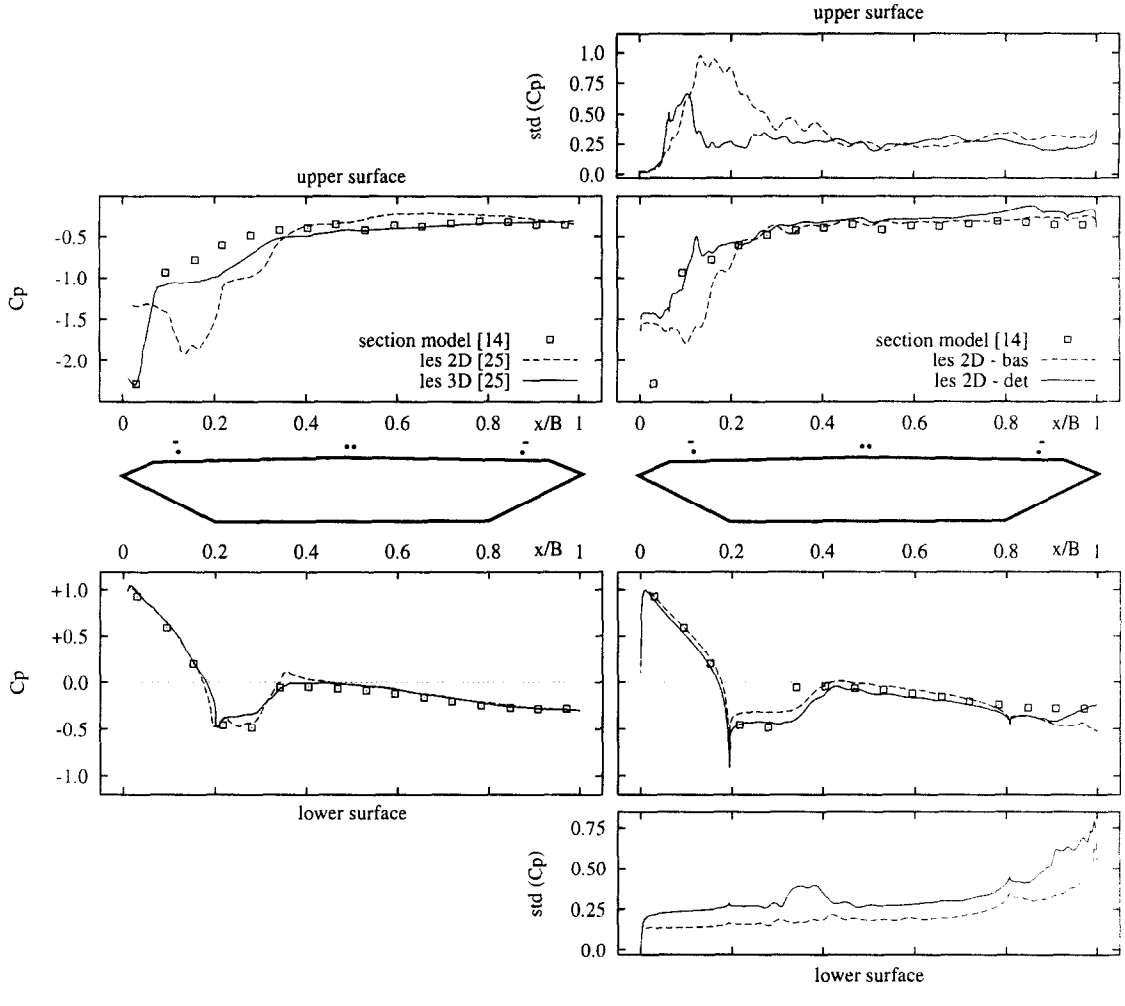

Figure 27. Cp and std (Cp) distributions on the basic and detailed deck $\alpha = +6°$.

The same setup was assumed by Enevoldsen *et al.* [25] in both 2D and 3D LES simulations using the Smagorinsky subgrid scale model. In the computational simulations, the turbulence level of the incoming flow was set at zero, and the value of the Smagorinsky constant was set at 0.18. Although Thorbek [28] states that the details were modelled in both 2D and 3D simulations, the local effects of the barriers cannot be found in the pressure distribution at the upper surface (see Figure 27a). The 3D simulation substantially improves the results obtained using the 2D model.

Figure 27b compares the results of the present study obtained using 2D models with and without barriers. It follows that an adequate value of the Smagorinsky constant and careful modelling of the details-combined with a numerical scheme and a refined grid yielding low dissipation-can overcome the limitations of 2D LES simulation. In particular, the 2D model ensures the same level of accuracy as 3D simulations, while the computational costs are considerably reduced.

5. CONCLUSIONS

The aim of the present paper has been to discuss the reliability of 2D numerical simulation of vortical structures around a quasi-bluff bridge deck.

The first part was devoted to a critical review of currently available studies on the topic.

This was followed by a closer investigation into the various mechanisms involved in the unsteady flow around the Great Belt East Bridge deck. The numerical simulations have shed some light

on the essential physical features of the process of vortex formation. In particular, the multiple Strouhal numbers experimentally measured were related to distinct vortex-shedding mechanisms.

The third part of the paper was devoted to a clarification, by means of a number of parametric studies, of the capacity of some models to simulate the case study. For each approach, the influence of a number of parameters of the computational model was examined. In the laminar approach, a reduced near-wall cell thickness and high-order diffusive schemes are required to calculate the flow field without dependence upon numerical diffusion.

Generally speaking, the ensemble-averaged models of the turbulence do not properly simulate the small-scale, complex eddies at the root of the vortex-formation process. The RANS equation models assume such eddies into the turbulent stochastic field. It follows that the augmented eddy viscosity markedly dissipates the periodic fluctuations.

Referring to the large eddy simulation approach, the relevance of using low-diffusive discretization schemes for the convective fluxes was confirmed by the parametric analysis reported in Section 4.3.1. Moreover, the influence of the value of the Smagorinsky constant in the subgrid scale model was studied in detail. The investigation makes it possible to fix an optimal value for this constant, enabling the LES 2D model to take into account the effects of physical phenomena (vortex stretching, longitudinal vortices) that are generally observed in the case of 3D separated flows with homogeneous spanwise fluctuations.

The overall accuracy of the optimised 2D model is comparable with the accuracy of 3D simulations, while the computational effort is considerably reduced. In principle, *a posteriori* error estimates can be developed exploiting the method by Diez and Egozcue [43]. Additional estimates concerning convergence and stability properties can be recovered in [44].

Finally, the important role of deck equipment in bridge aerodynamics is emphasized. Despite the increased computational effort, modelling of the barriers is strongly recommended in order to take into due account the global effects of the barriers on the flow.

Notwithstanding the encouraging results obtained in this study, caution must be exercised in extending the the proposed 2D LES approach to other classes of flow. The application of this approach to separated-type cylinder and streamlined sections represents a further possible research development.

REFERENCES

1. G. Buresti, Vortex-shedding from bluff bodies, In *Wind Effects on Buildings and Structures*, (Edited by Riera and Davemport), Balkema, Rotterdam, (1998).
2. H. Nakaguchi, K. Hashimoto and S. Muto, An experimental study on aerodynamic drag of rectangular cylinders, *J. Japan Soc. of Aeronautical and Space Sci.* **16** (168), 1–5, (1968).
3. K. Shimada and T. Ishihara Prediction of aeroelastic vibrations of rectangular cylinder by $k-\varepsilon$ model, *J. Aerospace Eng.* **4** (12), 122–135, (1999).
4. A. Okajima, Flow around a rectangular cylinder with a series of various width/height ratios, *J. Wind Eng.* **17**, 1–19, (1983).
5. N. Shiraishi and M. Matsumoto, On classification of vortex-induced oscillation and its application for bridge structures, *J. Wind Eng. Ind. Aerodyn.* **14**, 419–430, (1983).
6. J.H. Walter, Discrete vortex methods in bridge aerodynamics and prospects for parallel computing techniques, In *Bridge Aerodynamics*, (Edited by A. Larsen and S. Esdahl), pp. 301–311, Balkema, Rotterdam, (1998).
7. S. Murakami, W. Rodi, A. Mochida and S. Sakamoto, Large eddy simulation of vortex shedding flow past 2D square cylinder, *J. Wind Eng.* **55**, 79–80, (1993).
8. T. Tamura, I. Otha and K. Kuwahara, On the reliability of two-dimensional simulation for unsteady flows around a cylinder-type structure, *J. Wind Eng. Ind. Aerodyn.* **35**, 275–298, (1990).
9. S. Murakami and A. Mochida, On turbulent vortex-shedding flow past 2D square cylinder predicted by CFD, *J. Wind Eng. Ind. Aerodyn.* **54**, 191–211, (1995).
10. B. Bienkiewicz, Wind-tunnel study of geometry modification on aerodynamics of a cable-stayed bridge deck, *J. Wind Eng. Ind. Aerodyn.* **26**, 325–339, (1987).
11. R.H. Scanlan, N.P. Jones, P.P. Sarkar and L. Singh, The effect of section model details on aeroelastic parameters, *J. Wind Eng. Ind. Aerodyn.* **54/55**, 45–53, (1995).
12. L. Bruno, S. Khris and M. Marcillat, Numerical simulation of the effect of section details and partial streamlining on the aerodynamics of a long-span bridge deck, *Wind and Structures* **4**, 315–332, (2001).

13. A. Larsen, Aerodynamic aspects of the final design of the 1624-m suspension bridge across the Great Belt, *J. Wind Eng. Ind. Aerodyn.* **48**, 261–285, (1993).
14. T.A. Reinhold, M. Brinch and A. Damsgaard, Wind-tunnel tests for the Great Belt Link, In *Aerodynamics of Large Bridges*, (Edited by A. Larsen), pp. 255–267, Balkema, Rotterdam, (1992).
15. G.L. Larose, The response of a suspension bridge deck to the turbulent wind: The taut-strip model approach, *M. Eng. Sc.*, The University of Western Ontario, Ontario, (1992).
16. J.B. Frandsen, Simultaneous pressures and accelerations measured full-scale on the Great Belt East suspension bridge, *J. Wind Eng. Ind. Aerodyn.* **89** (1), 95–129, (2001).
17. A. Larsen and J.H. Walter, Aeroelastic analysis of bridge girder sections based on discrete vortex simulations, *J. Wind Eng. Ind. Aerodyn.* **67/68**, 253–265, (1997).
18. A. Larsen and S. Esdahl, Discrete vortex simulations of fluid-structure interaction in bridge engineering, In *Computational Methods for Fluid-Structure Interaction*, (Edited by T. Kvamsdal), Tapir Forlag, Trondheim, (1999).
19. I.J. Taylor and M. Vezza, Analysis of the wind loading on bridge-deck sections using a discrete vortex method, In *Wind Engineering into the 21st Century*, (Edited by A. Larsen *et al.*), pp. 1345–1352, Balkema, Rotterdam, (1999).
20. J.B. Frandsen, Comparison of numerical predictions and full-scale measurements of vortex-induced oscillations, In *Proc. 4th International Colloquium on Bluff Body Aerodynamics & Applications*, (Edited by H.J. Niemann *et al.*), Ruhr-University of Bochum, Bochum, (2000).
21. S. Kuroda, Numerical simulation of flow around a box girder of a long-span suspension bridge, *J. Wind Eng. Ind. Aerodyn.* **67/68**, 239–252, (1997).
22. R. Panneer Selvam and H.R. Bosch, Finite-element modelling of flow around bridges, In *Wind Engineering into the 21st Century*, (Edited by A. Larsen *et al.*), pp. 1321–1327, Balkema, Rotterdam, (1999).
23. R.P. Selvam, Computational procedures in grid-based computational bridge aerodynamics, In *Bridge Aerodynamics*, (Edited by A. Larsen and S. Esdahl), pp. 327–336, Balkema, Rotterdam, (1998).
24. C.B. Jenssen and T. Kvamsdal, Computational methods for FSI simulations of slender bridges on high performance computers, In *Computational Methods for Fluid-Structure Interaction*, (Edited by T. Kvamsdal), Tapir Forlag, Trondheim, (1999).
25. I. Enevoldsen, C. Pedersen, S.O. Hansen, T.L. Thorbek and T. Kvamsdal, Computational wind simulations for cable-supported bridges, In *Wind Engineering into the 21st Century*, (Edited by A. Larsen *et al.*), pp. 1265–1270, Balkema, Rotterdam, (1999).
26. M. Pecora, L. Lecce, F. Marulo and D.P. Coiro, Aeroelastic behaviour of long-span bridges with "multibox" type deck sections, *J. Wind Eng. Ind. Aerodyn.* **48**, 343–358, (1993).
27. J.B. Frandsen and F.A. McRobie, Computational aeroelastic modelling to guide long-span bridge cross-section design, In *Wind Engineering into the 21st Century*, (Edited by A. Larsen *et al.*), pp. 1277–1284, Balkema, Rotterdam, (1999).
28. T.L. Thorbek, Numerical simulations of the vortex shedding past the Great Belt East Bridge deck, Private communications, (2001).
29. T. Sarpkaya, Computational methods with vortices—The 1988 Freeman scholar lecture, *ASME J. Fluids Eng.* **111**, 5–52, (1989).
30. S. Lee, J.S. Lee and J.D. Kim, Prediction of vortex-induced wind loading on long-span bridges, *J. Wind Eng. Ind. Aerodyn.* **67/68**, 267–278, (1997).
31. R. Franke and W. Rodi, Calculation of vortex shedding past a square cylinder with various turbulence models, In *Proc. Eighth Symposium on Turbulent Shear Flows*, pp. 20-1-1–20-1-6, Technical University of Munich, Munich, (1991).
32. B.E. Launder and D.B. Spalding The numerical computation of turbulent flows, *Computer Methods in Applied Mechanics and Engineering* **3**, 269–289, (1974).
33. V. Yakhot, S.A. Orszag, S. Thangam, T.B. Gatski and G.C. Speziale, Development of turbulence models for shear flows by a double expansion technique, *Phys. Fluids* **A4** (7), 1510–1520, (1992).
34. F.S. Lien and M.A. Leschziner, Assessment of turbulent transport models including nonlinear RNG eddy viscosity formulation and second-moment closure, *Computers Fluids* **23** (8), 983–1004, (1994).
35. M.M. Gibson and B.E. Launder, Ground effects on pressure fluctuations in the atmospheric boundary layer, *J. Fluid Mech.* **86**, 491–511, (1978).
36. J. Smagorinsky, General circulation experiments with the primitive equations. I. The basic experiment, *Month. Weather Rev.* **91**, 99–164, (1963).
37. H.C. Chen and V.C. Patel, Near-wall turbulence models for complex flows including separation, *AIAA Journal* **26** (6), 641–648, (1988).
38. R.I. Issa, Solution of implicitly discretized fluid-flow equations by operator splitting, *J. Comput. Phys.* **62**, 40–65, (1986).
39. R.F. Warming and R.M. Beam, Upwind second-order difference schemes and application in aerodynamic flows, *AIAA Journal* **9** (14), 1241–1249, (1976).
40. B.P. Leonard, A stable and accurate convective modelling procedure based on quadratic upstream interpolation, *Comp. Meth. Appl. Mech. Eng.* **19**, 59–98, (1979).
41. W. Shyy, S. Thakur and J. Wright, Second-order upwind and central difference schemes for recirculating flow computation, *AIAA Journal* **4** (30), 923–932, (1992).

42. M. Breuer, Numerical and modelling influences on large-eddy simulation for the flow past a circular cylinder, In *Proc. 11th Symposium on Turbulent Shear Flows*, Grenoble, (1997).
43. P. Diez and J.J. Egozcue, Probabilistic analysis of an *a posteriori* error estimator for finite elements, *Mathematical Models and Methods in Applied Sciences* **5** (11), 841–854, (2001).
44. K. Gerdes, J.M. Melenk, C. Schwab and D. Schötzau, The hp-version of the streamline diffusion finite element method in two space dimensions, *Mathematical Models and Methods in Applied Sciences* **2** (11), 301–337, (2001).